

# Chemical abundances of LINER galaxies - Nitrogen abundance estimations

C. B. Oliveira Jr.<sup>1\*</sup>, A.C. Krabbe<sup>2†</sup>, O. L. Dors Jr.<sup>1</sup>, I. A. Zinchenko<sup>3,4</sup>,  
J. A. Hernandez-Jimenez<sup>1</sup>, M. V. Cardaci<sup>5</sup>, G. F. Hägele<sup>5</sup>, G. S. Ilha<sup>2</sup>

<sup>1</sup> Universidade do Vale do Paraíba, Av. Shishima Hifumi, 2911, Zip Code 12244-000, São José dos Campos, SP, Brazil

<sup>2</sup> Universidade de São Paulo, Instituto de Astronomia, Geofísica e Ciências Atmosféricas, Rua do Matão 1226, CEP 05508-090, São Paulo, SP, Brazil

<sup>3</sup> Faculty of Physics, Ludwig-Maximilians-Universität, Scheinerstr. 1, 81679 Munich, Germany

<sup>4</sup> Main Astronomical Observatory, National Academy of Sciences of Ukraine, 27 Akad. Zabolotnogo St 03680 Kyiv, Ukraine

<sup>5</sup> Instituto de Astrofísica de La Plata (CONICET–UNLP), Paseo del Bosque s/n, B1900FWA La Plata, Argentina.

Accepted XXX. Received YYY; in original form ZZZ

## ABSTRACT

In this work, we investigated the nitrogen and oxygen abundances in a sample of galaxies with Low Ionization Nuclear Emission Regions (LINERs) in their nucleus. Optical spectroscopic data (3 600 - 10 000 Å) of 40 LINERs from the Mapping Nearby Galaxies (MaNGA) survey were considered. Only objects classified as retired galaxies, i.e. whose main ionization sources are post-Asymptotic Giant Branch (pAGB) stars, were selected. The abundance estimates were obtained through detailed photoionization models built with the CLOUDY code to reproduce a set of observational emission line intensities ratios of the sample. Our results show that LINERs have oxygen and nitrogen abundances in the ranges of  $8.0 \lesssim 12 + \log(\text{O}/\text{H}) \lesssim 9.0$  (mean value  $8.74 \pm 0.27$ ) and  $7.6 \lesssim 12 + \log(\text{N}/\text{H}) \lesssim 8.5$  (mean value  $8.05 \pm 0.25$ ), respectively. About 70% of the sample have oversolar O/H and N/H abundances. Our abundance estimates are in consonance with those for Seyfert 2 nuclei and H II regions with the highest metallicity, indicating that these distinct object classes show similar enrichment of the interstellar medium (ISM). The LINERs in our sample are located in the higher N/O region of the N/O versus O/H diagram, showing an unexpected negative correlation between these two parameters. These results suggest that these LINERs mainly exhibit a secondary nitrogen production and could be acting some other mechanisms that deviate them from the usual theoretical secondary nitrogen production curve and the H II regions observations. However, we did not find any evidence in our data able to support the literature suggested mechanisms. On the other hand, our results show that LINERs do not present any correlation between the N/O abundances and the stellar masses of the hosting galaxies.

**Key words:** galaxies:abundances – ISM:abundances – galaxies:nuclei

## 1 INTRODUCTION

Estimations of chemical abundances of the gas phase of Active Galactic Nuclei (AGNs) and star-forming (SF) regions (H II regions and H II galaxies) are fundamental to understanding the chemical evolution of galaxies along the history of the Universe. The spectra of these objects present strong emission lines that are easily detectable, even in objects at (very) high redshift ( $z = \sim 1.0 - \sim 9.0$ ) (e.g., Curti et al. 2023; Sanders et al. 2023), and these lines can be used to estimate the metallicity ( $Z$ ) and other properties (e.g., electron density, elemental abundance, hardness of the ionizing spectra,

etc) of these objects (for a review see Maiolino & Mannucci 2019; Kewley et al. 2019).

Generally, the gas-phase metallicity is traced through the oxygen abundance in relation to the hydrogen (O/H), due to the oxygen has strong emission lines in the optical spectrum ([O II] $\lambda$ 3726,  $\lambda$ 3729, [O III] $\lambda$ 5007) emitted by its more abundant ions ( $\text{O}^+$ ,  $\text{O}^{2+}$ ). Therefore, hereafter we use metallicity ( $Z$ ) and oxygen abundance (O/H) interchangeably. It is largely accepted that the most reliable method to estimate O/H and the abundance of other elements (e.g., N, S, Ne) is the  $T_e$ -method (see discussion in Hägele et al. 2006, 2008)<sup>1</sup>. The reliability of the  $T_e$ -method is supported by the agreement between O/H estimates in H II regions

\* E-mail: cbo\_jr@hotmail.com (CBO)

† E-mail: angela.krabbe@gmail.com (ACK)

<sup>1</sup> For a review of the  $T_e$ -method see Peimbert et al. (2017) and Pérez-Montero (2017).

and those in neighborhood stars (see Pilyugin 2003; Toribio San Cipriano et al. 2017). The  $T_e$ -method is based on determinations of electron temperatures and requires measurements of auroral emission lines, such [O III] $\lambda$ 4363 and [N II] $\lambda$ 5755, which are weak (about 100 times weaker than H $\beta$ ) or even not detectable in most parts of objects with high metallicity and/or low excitation (van Zee et al. 1998; Díaz et al. 2007; Dors et al. 2008). In the cases in which the  $T_e$ -method can not be applied, Z and elemental abundances (e.g., N/H, S/H) have been estimated through calibrations between these and intensities of strong emission line ratios (hereafter strong-line method) of SF regions (e.g., Pagel et al. 1979; Alloin et al. 1979; McGaugh 1991; Thurston et al. 1996; Christensen et al. 1997; Díaz & Pérez-Montero 2000; Oey & Shields 2000; Kewley & Dopita 2002; Pettini & Pagel 2004; Pérez-Montero et al. 2006; Stasińska 2006; Nagao et al. 2006; Yin et al. 2007; Viironen et al. 2007; Shi et al. 2007; Dopita et al. 2013; Marino et al. 2013; Morales-Luis et al. 2014; Jones et al. 2015; Brown et al. 2016; Pilyugin & Grebel 2016; Curti et al. 2017; Hirschauer et al. 2018; Jiang et al. 2019; Ho 2019; Mingozi et al. 2020; Pérez-Montero et al. 2021; Florido et al. 2022; Díaz & Zamora 2022) and AGNs (Storchi-Bergmann et al. 1998; Castro et al. 2017; Carvalho et al. 2020; Dors 2021; Dors et al. 2021).

The vast spectroscopic optical data obtained by surveys – e.g., data made available by the Sloan Digital Sky Survey (SDSS, York et al. 2000), Calar Alto Legacy Integral Field Area (CALIFA, Sánchez et al. 2012), Mapping Nearby Galaxies at Apache Point Observatory (MaNGA, Bundy et al. 2015), and Chemical Abundances of Spirals (CHAOS, Berg et al. 2015) – have revolutionized the understanding of the chemical enrichment of SF regions (e.g., Tremonti et al. 2004; Izotov et al. 2006, 2019; Sánchez et al. 2014; Belfiore et al. 2017; Berg et al. 2020; Rogers et al. 2022, among others) in the local universe. However, estimations of the metallicity and elemental abundances in other object classes, such as AGNs and Low Ionization Nuclear Emission-line Region (LINERs) are little known. For instance, the first quantitative determination of the N/H abundance in AGNs (Seyfert 2 type) was only performed recently by Dors et al. (2017). These authors used detailed photoionization models to reproduce the optical spectrum of 44 Seyfert 2s in the local ( $z < 0.1$ ) universe (see also Pérez-Montero et al. 2019; Flury & Moran 2020). Moreover, neon, argon, helium, and sulfur abundances have also been recently estimated in a small sample (less than 70 objects,  $z < 0.3$ ) of AGNs by Armah et al. (2021), Monteiro & Dors (2021) and Dors et al. (2022, 2023), respectively.

A worse scenario is found for LINERs, despite these objects appearing in  $\sim 1/3$  of galaxies in the local universe (Netzer 2013). This fact is possibly due to the need to know the nature of the ionizing sources and excitation mechanisms of LINERs in order to apply the  $T_e$ -method (Dors et al. 2020) and/or strong-line methods (Storchi-Bergmann et al. 1998). Annibali et al. (2010), using optical spectra of a sample of LINERs located in early-type galaxies (ETGs), estimated the O/H abundance assuming hot stars and the accretion of gas into a central black hole (AGN) as ionization sources. The authors found that the average abundance obtained from AGN calibration is  $\sim 0.05$  dex higher than those obtained through hot stars calibration, however, the last one produced a broader metallicity range. Krabbe et al. (2021) derived the O/H abundance of the UGC 4805 LINER nucleus using MaNGA data and using distinct methods, i.e., the extrapolation of the disk abundance gradient, the calibrations between O/H abundance and strong emission lines for AGNs, as well as photoionization models built with the CLOUDY code (Ferland et al. 2017), assuming gas accretion into a black hole (AGN) and post-asymptotic giant branch (pAGB) stars with different effective

temperatures. These authors found that depending on the method adopted, discrepancies of until  $\sim 0.4$  dex are derived (see Table 2 of Krabbe et al. 2021). Finally, Oliveira et al. (2022) proposed, for the first time, two semi-empirical calibrations based on photoionization models to estimate the oxygen abundance of LINERs as a function of intensities of strong optical emission-line ratios. These authors were able to estimate the O/H abundance for 43 LINERs classified as retired galaxies, i.e., ionized by pAGB stars, finding values in the range  $8.5 \lesssim 12 + \log(\text{O}/\text{H}) \lesssim 8.9$ , or  $0.6 \lesssim (Z/Z_\odot) \lesssim 1.4$  assuming the solar oxygen value  $12 + \log(\text{O}/\text{H}) = 8.69$  (Allende Prieto et al. 2001).

The determination of the abundance of other elements, such as N and S, is barely found in the literature for LINERs. Indeed, the only available abundance estimation of other heavy elements for LINERs was performed by Pérez-Díaz et al. (2021). In this study was determined the nitrogen-to-oxygen abundance ratio for a sample of 40 LINERs using the HII-CHI-MISTRY code (Pérez-Montero 2014; Pérez-Montero et al. 2019). This code performs a Bayesian-like comparison between the predictions from certain optical emission-line ratios and a large grid of photoionization models that assumes AGNs as ionization sources. They found that LINERs present N/O abundance ratio values similar to SF regions, but lower ( $\sim 0.20$  dex) than those of Seyfert 2 nuclei. The objects considered by Pérez-Díaz et al. (2021) were classified as LINERs through two classical emission line ratio diagnostic diagrams, i.e., [O III] $\lambda$ 5007/H $\beta$  versus [S II] $(\lambda$ 6716+ $\lambda$ 6731)/H $\alpha$  and versus [O I] $\lambda$ 6300/H $\alpha$ . However, these diagrams can not discriminate the ionization source of the LINERs. In fact, a gas excited by an AGN, shocks, or pAGB stars occupies similar regions in classical optical diagnostic diagrams (e.g., Dors et al. 2021; Lagos et al. 2022; Feltre et al. 2023), requiring additional analysis to carry out galaxy spectral classification (e.g., Stasińska et al. 2008; Panuzzo et al. 2011; Juneau et al. 2011; Shirazi & Brinchmann 2012; Ricci et al. 2014; Rich et al. 2014; Bär et al. 2017; Davies et al. 2017; Wylezalek et al. 2018; Byler et al. 2019; Agostino & Salim 2019). It is crucial to note that classical diagnostic diagrams (Baldwin et al. 1981; Veilleux & Osterbrock 1987) alone can not distinguish the ionization source of LINERs; whether it is due to AGNs, shocks, or pAGB stars. Therefore, an additional analysis is required to determine the ionization source of LINERs. In this sense, the WHAN diagram proposed by Cid Fernandes et al. (2010), which takes into account the equivalent width of H $\alpha$  ( $EW_{\text{H}\alpha}$ ) versus [N II] $\lambda$ 6584/H $\alpha$  line ratio, is a useful tool to differentiate the nature of the ionization sources of the objects classified previously as LINER in the BPT diagram, i.e., between evolved low-mass stars (like pAGB stars) and low ionization AGNs.

Nitrogen is predominantly produced in stars with low and intermediate-mass through two distinct nucleosynthetic processes: primary and secondary. The primary mechanism was initially proposed by Truran & Cameron (1971) and later expanded upon by Talbot & Arnett (1974). In this production mechanism, nitrogen arises from intermediate-mass stars, within the mass range  $4 \lesssim M_* \lesssim 8M_\odot$ , with a smaller contribution from massive stars ( $M_* \gtrsim 8M_\odot$ ) through nuclear reactions involving only the H and He. Additionally, Meynet & Maeder (2002) have suggested that N can also be primarily produced by massive stars with very low metallicity and higher rotation, particularly during the thermal pulse phases of asymptotic giant branch (AGB) stars. On the other hand, secondary nucleosynthesis is explained through the Carbon-Nitrogen-Oxygen (CNO) cycle, where nitrogen is a product of nuclear reactions involving carbon and oxygen. Several studies have explored this secondary process (e.g. Johnson et al. 2023; Grisoni et al. 2021; Johnson 2019; Vin-

cenzo & Kobayashi 2018; Wu & Zhang 2013; Thuan et al. 2010; Pilyugin et al. 2003; Henry et al. 2000; Matteucci 1986).

One important relation that has been investigated by several authors is the nitrogen-to-oxygen ratio, as it exhibits a direct correlation with variations in metallicity and the star formation history (e.g., Contini 2017; Maiolino & Mannucci 2019). Usually, the *N/O versus O/H metallicity diagram* exhibits a clear behavior: a plateau at low-metallicity regime ( $12 + \log(O/H) \lesssim 8.4$ , see e.g., Andrews & Martini 2013; Berg et al. 2019), that represents the primary nucleosynthesis of the nitrogen, changing abruptly the slope at O/H in the higher metallicity regime, interpreting as the secondary production of the nitrogen (e.g., Edmunds & Pagel 1978; Matteucci 1986; Vincenzo et al. 2016). Specifically, as the nitrogen abundance increases with the C and O abundances, at high metallicities, the nitrogen abundance is expected to evolve quadratically with metallicity, expressed as  $N/O \propto O/H$  or, equivalently,  $N/H \propto (O/H)^2$  (see Maiolino & Mannucci 2019).

In this study, the third a series (Paper I - Krabbe et al. 2021 and Paper II - Oliveira et al. 2022), we investigate the nitrogen and oxygen abundances of 43 LINERs. The ionization sources of these LINERs were previously classified as pAGB stars by Oliveira et al. (2022). We carried out this analysis using the CLOUDY code (Ferland et al. 2017) to build detailed photoionization models to reproduce strong optical emission line ratios found for the objects in our sample and, thus, estimate the N/H and O/H abundances. We follow a similar methodology as the one applied by Dors et al. (2017) to estimate the abundances in a sample of Seyfert 2 nuclei. This paper is organized as follows: Section 2 describes the observational data. In Section 3 we present the photoionization model descriptions and the methodology applied to derive the nitrogen and oxygen abundance. In Section 4 the results and discussions are shown, while in Section 5 we present our conclusions.

## 2 OBSERVATIONAL DATA

To derive the nitrogen and oxygen abundances, observational optical emission-line intensities of LINER nuclei taken from the MaNGA survey (Bundy et al. 2015) were considered. The spectra comprehend the wavelength range of 3 600 - 10 000 Å, with a spatial resolution of about 2.5 arcsec (Smee et al. 2013; Wake et al. 2017). Auroral emission lines, such as  $[O III]\lambda 4363$ , are not detected. Therefore, our analysis exclusively considers only strong emission lines —  $[O II]\lambda 3727$ ,  $[O III]\lambda 5007$ ,  $[N II]\lambda 6584$ ,  $[S II]\lambda 6717$ , 6731,  $H\alpha$ , and  $H\beta$  — measured with a signal-to-noise ratio higher 3. These emission lines have been corrected by reddening using the extinction curve by Cardelli et al. (1989), which is widely used as a reference for the internal extinction curve in the local universe galaxies (Salim & Narayanan 2020). The sample of objects is the same as selected by Oliveira et al. (2022) and is composed of 43 galaxies with LINER emission in their nuclear region and with SF emission in their disks. A detailed description of the data reduction, reddening correction procedure, etc., are presented in Oliveira et al. (2022). The selection criteria are summarized in what follows.

- Initially, we used the  $[O III]\lambda 5007/H\beta$  versus  $[N II]\lambda 6584/H\alpha$  diagnostic diagram proposed by Baldwin et al. (1981), known as  $[N II]$ -diagram, to classify each spaxel of the individual objects as H II-like regions or AGN-like objects. For that, we assumed the theoretical and empirical criteria proposed by Kewley et al. (2001)

and Kauffmann et al. (2003), respectively, and given by:

$$\log([O III]\lambda 5007/H\beta) > \frac{0.61}{\log([N II]\lambda 6584/H\alpha) - 0.47} + 1.19 \quad (1)$$

and

$$\log([O III]\lambda 5007/H\beta) > \frac{0.61}{\log([N II]\lambda 6584/H\alpha) - 0.05} + 1.3. \quad (2)$$

The AGN-like objects were discerned into Seyfert and LINER categories using the criteria outlined by Cid Fernandes et al. (2010):

$$\log([O III]\lambda 5007/H\beta) < 0.48 + 1.01 \times \log([N II]\lambda 6584/H\alpha). \quad (3)$$

- Taking into account the spaxels classified as LINER in the  $[N II]$ -diagram, we applied the WHAN [ $\log(EW_{H\alpha})$  versus  $\log([N II]\lambda 6584)$ ] diagram (Cid Fernandes et al. 2011) to differentiate the nature of the ionization sources of the objects, i.e. between evolved low-mass stars (like post-AGB stars) and low ionization AGNs. We only selected spaxels classified as Retired Galaxies (RG), i.e.  $EW_{H\alpha} < 3 \text{ \AA}$ , suggesting that the ionization sources are probably post-AGB stars.

- After the previous classification processes, performed on each individual spaxel, we integrated the fluxes within a circular aperture with a radius of 1 kpc located at the nuclear region of each galaxy. For these integrated regions we applied the same classification based on the  $[N II]$ -diagram and the WHAN diagrams.

- Finally, we selected all the galaxies whose integrated nuclear emission is simultaneously classified as LINER in the  $[N II]$ -diagram and as RG in the WHAN diagram. In Figure 1 both diagnostic diagrams are shown. For the  $[N II]$ -diagram, we considered an error of  $\pm 0.1$  dex for the criterion by Kewley et al. (2001) to separate AGN-like and H II-like objects, and the same error value for the criterion by Cid Fernandes et al. (2010) to distinguish Seyfert and LINER objects.

The stellar mass of the hosting galaxies is in the range of  $10 \lesssim \log(M_*/M_\odot) \lesssim 11.2$  and the redshift is in the range of  $0.02 \lesssim z \lesssim 0.07$ . In Table 1 the observational emission-line intensities (in relation to  $H\beta$ ) of the objects for which we were able to reproduce their emission-line ratios (see below) are listed. In the first column of this table is also given the MaNGA identifier "plate-IFU" for each object.

## 3 PHOTOIONIZATION MODELS

### 3.1 Initial parameters

Individual photoionization models, built with the CLOUDY code version 17.02 (Ferland et al. 2017), were used to reproduce the observed emission line intensities (in relation to  $H\beta$ ) for each object of our sample. Initial parameters for each model were derived following the methodology described below.

(i) Ionization parameter: the logarithm of the ionization parameter ( $\log U$ ) was derived by the equation proposed by Oliveira et al. (2022):

$$\log U = 0.57(\pm 0.01)x - 3.19(\pm 0.01),$$

being  $x = \log([O III]\lambda 5007/[O II]\lambda 3727)$  obtained from the observational data. A plane-parallel geometry was assumed in the models (see the discussion by Oliveira et al. 2022 about the selection of this parameter).

**Table 1.** Dereddened fluxes (relative to  $H\beta=1.00$ ) for our sample of LINER nuclei. The observed values compiled from the literature are referred as "Obs." while the predicted values by the photoionization models as "Mod." (see Sect.3).

Object	[O II] $\lambda$ 3727		[O III] $\lambda$ 5007		[N II] $\lambda$ 6584		[S II] $\lambda$ \lambda6716+31		H $\alpha$	
	Obs.	Mod.	Obs.	Mod.	Obs.	Mod.	Obs.	Mod.	Obs.	Mod.
7495-12704	1.77	1.91	1.79	1.70	3.25	3.31	2.08	2.04	2.87	2.83
7977-3704	5.06	6.08	1.65	1.74	2.73	2.60	1.90	1.67	2.87	2.85
7977-12703	3.93	4.81	1.31	1.30	2.54	2.40	1.88	1.93	2.87	2.82
7990-12704	4.35	4.48	2.10	2.09	3.01	3.08	3.08	3.21	2.87	2.81
8083-12704	2.27	2.54	1.32	1.26	2.90	2.83	2.78	2.56	2.87	2.82
8140-12703	8.77	9.56	1.87	1.80	3.23	3.37	1.89	1.88	2.87	2.80
8247-3701	3.58	3.65	1.44	1.52	3.06	3.17	1.67	1.72	2.87	2.81
8249-12704	4.25	4.07	3.88	4.03	3.45	3.15	2.36	2.38	2.87	2.81
8254-3704	5.62	5.92	2.04	2.11	3.25	3.41	2.22	2.35	2.87	2.80
8257-1902	3.90	4.85	1.40	1.38	2.77	2.73	1.88	1.85	2.87	2.85
8259-9102	8.45	8.29	2.44	2.47	3.08	3.04	1.63	1.62	2.87	2.79
8313-9102	5.05	4.98	2.30	2.15	4.32	4.49	3.04	3.16	2.87	2.80
8313-12705	5.55	5.64	3.16	3.17	4.02	4.01	3.34	3.46	2.87	2.80
8318-12703	4.19	4.85	2.77	2.35	4.02	4.13	2.85	3.03	2.87	2.81
8320-9102	4.70	4.22	2.81	2.51	3.82	3.75	2.30	2.28	2.87	2.81
8330-9102	2.29	2.38	1.82	1.77	3.63	3.60	2.52	2.47	2.87	2.82
8332-6103	7.97	8.23	3.84	4.03	3.40	3.45	2.28	2.39	2.87	2.79
8440-12704	3.82	4.05	1.71	1.56	3.23	3.24	3.25	2.94	2.87	2.82
8481-1902	6.57	6.74	2.17	2.23	3.00	3.01	2.26	2.23	2.87	2.80
8482-12703	10.04	10.40	4.10	4.19	5.17	5.24	2.72	2.71	2.87	2.79
8550-6103	4.73	5.21	1.53	1.59	3.13	3.22	2.59	2.67	2.87	2.84
8550-12705	9.88	11.26	3.98	4.13	3.71	3.81	1.67	1.63	2.87	2.81
8552-9101	6.49	6.15	1.43	1.45	3.71	3.82	2.31	2.43	2.87	2.81
8601-12705	3.48	4.20	1.51	1.52	2.54	2.54	1.55	1.54	2.87	2.88
8588-9101	3.89	4.62	1.20	1.19	2.62	2.63	1.59	1.61	2.87	2.85
8138-9101	6.30	6.18	2.32	2.24	3.04	3.03	1.14	1.14	2.87	2.81
8482-9101	6.56	6.72	5.51	5.84	4.15	4.09	2.16	2.15	2.87	2.79
8554-1902	4.16	4.41	3.00	3.08	2.70	2.71	2.55	2.42	2.87	2.79
8603-12703	1.86	2.00	1.14	1.16	2.41	2.35	1.93	1.83	2.87	2.83
8604-6102	5.46	5.37	2.87	2.71	3.91	3.82	3.59	3.44	2.87	2.80
8606-3702	8.84	8.90	4.00	4.29	3.63	3.80	3.18	3.41	2.87	2.80
7990-6103	11.40	10.90	2.71	2.69	2.57	2.60	2.43	2.50	2.87	2.85
8243-9102	10.61	10.33	3.09	3.10	6.39	6.51	1.97	2.11	2.87	2.82
8243-12701	12.46	12.20	4.26	4.31	4.08	4.11	1.92	1.96	2.87	2.79
8332-12705	18.37	14.63	4.46	4.40	4.46	4.48	2.08	1.97	2.87	2.83
8549-3703	16.61	14.03	4.88	5.02	3.96	3.77	2.77	3.06	2.87	2.83
8550-12704	10.91	10.56	2.93	2.95	4.77	4.72	3.08	3.11	2.87	2.82
8138-3702	13.32	13.66	3.98	4.05	3.86	3.71	3.76	3.56	2.87	2.80
8482-3704	10.00	9.17	2.03	2.11	3.67	3.61	1.95	2.02	2.87	2.80
8604-12703	12.39	12.17	5.35	5.29	5.23	5.33	2.64	2.65	2.87	2.82

(ii) Spectral energy distribution (SED): we assumed the SED represented by a post-AGB star atmosphere model by [Rauch \(2003\)](#), with the logarithm of the surface gravity  $\log(g) = 6$  and an effective temperature of  $T_{\text{eff}} = 190$  kK.

(iii) Electron density ( $N_e$ ): we assumed a constant  $N_e$  value along the nebular radius. For each object,  $N_e$  was derived through the observational  $[S II]\lambda 6716/\lambda 6731$  line ratio, assuming an electron temperature equal to 10 000 K, which is a representative value for H II regions (e.g. [Kennicutt et al. 2003](#); [Berg et al. 2020](#)), and by using the TEMDEN task of the IRAF software. It was possible to derive  $N_e$  for 24 objects. For the remaining of the galaxies in the sample, we were not able to directly derive  $N_e$  due to the [S II] line ratio being higher than  $\sim 1.4$  (see [Osterbrock 1989](#)). Therefore, for the latter, we considered  $N_e = 400 \text{ cm}^{-3}$  as the initial value. This value is the average  $N_e$  obtained from the objects for which we were able to derive  $N_e$  through the [S II] line ratio.

(iv) Metallicity ( $Z$ ): the value of the oxygen abundance for each

object was derived through the semi-empirical calibration proposed by [Oliveira et al. \(2022\)](#):

$$12 + \log(O/H) = 0.71(\pm 0.03)N2 + 8.58(\pm 0.01),$$

being  $N2 = \log([N II]\lambda 6584/H\alpha)$  obtained from the observational data. To convert the oxygen abundance into metallicity we applied the following:

$$(Z/Z_{\odot}) = 10^{8.69 - [12 + \log(O/H)]}$$

being 8.69 dex the solar oxygen abundance ([Allende Prieto et al. 2001](#)). Following [Dors et al. \(2017\)](#), models are assumed to be dust-free. The effects of the presence of dust in the gas phase on the inferred N and O abundances are discussed in Sec. 4.1. It is important to note that the solar abundances of O, N, and S correspond to the default values defined in the CLOUDY version utilized

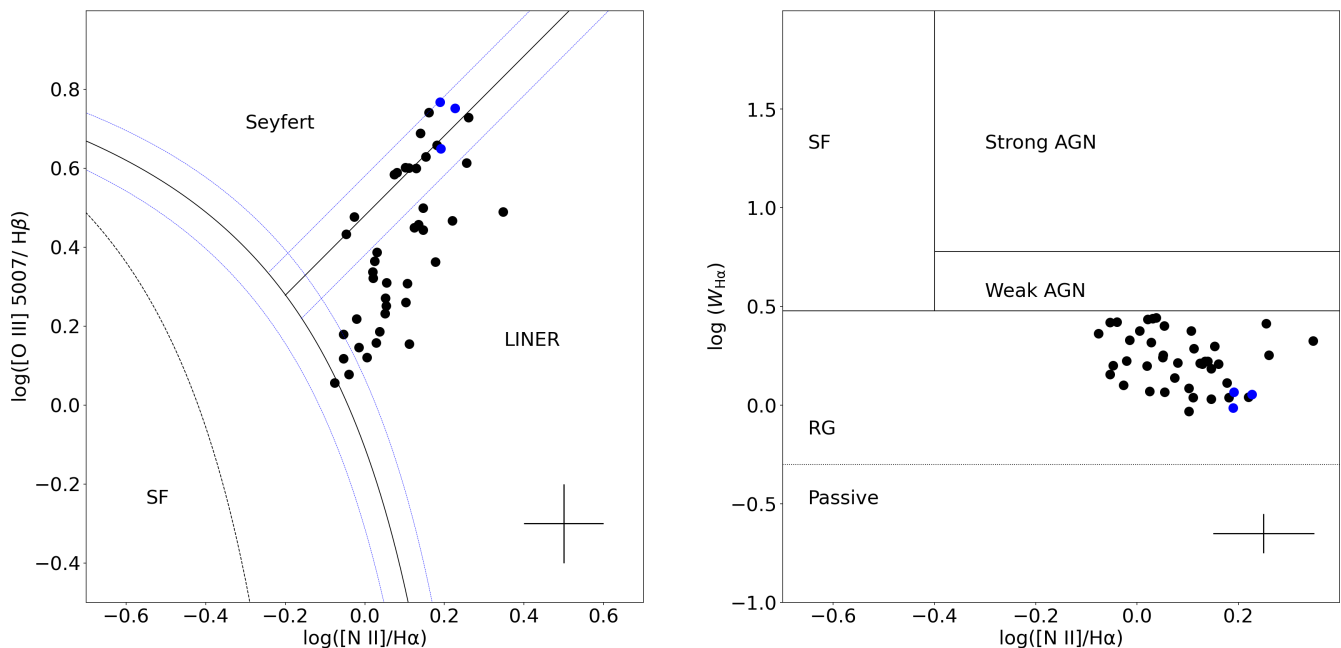


**Figure 1.** Left panel:  $[\text{O III}]\lambda 5007/\text{H}\beta$  vs.  $[\text{N II}]\lambda 6584/\text{H}\alpha$  diagnostic diagram. The black solid curve represents the theoretical separation between H II-like and AGN-like objects proposed by Kewley et al. (2001); the dashed black curve is the empirical star-forming limit proposed by Kauffmann et al. (2003), and the black solid line, proposed by Cid Fernandes et al. (2010), represents the separation between Seyferts and LINERs. The error bars represent the typical uncertainties of  $\pm 0.1$  dex in emission line measurements (see Oliveira et al. 2022 for a description of fluxes measurements and uncertainties estimations). Blue dashed lines represent the assumed error of  $\pm 0.1$  dex, as explained in Section 2. Black points represent the nuclear-integrated flux for each galaxy in our sample. Right panel: WHAN diagnostic diagram. Blue points in both panels are the galaxies for which we could not reproduce the observed emission line intensities by our models (see Sec. 4).

for constructing the photoionization models (Table 7.1 of CLOUDY manual HAZY 1<sup>2</sup>).

### 3.2 Fitting model methodology

For each galaxy in our sample, we built an initial model with the input parameters as previously mentioned to reproduce the observational emission line intensities. Then, new models were built varying, separately,  $Z$ ,  $N/\text{H}$ ,  $S/\text{H}$ ,  $T_{\text{eff}}$ , and  $\log U$ , considering a step of  $\pm 0.2$  dex, the typical uncertainties in nebular parameter estimations derived through photoionization models (see e.g., Dors et al. 2011).

In particular, some uncertainty in the measured flux of  $[\text{S II}]$  emission lines in our sample is obtained due to the contribution of the diffuse ionized gas (DIG, see Kumari et al. 2019 and references therein), which increases with the decrease of the  $\text{H}\alpha$  surface brightness of galaxies (e.g., Oey et al. 2007; Zhang et al. 2017). In fact, Pérez-Montero et al. (2023), who used the HCM-TEFF code<sup>3</sup> to constraint physical parameters of SF regions, found that diagrams assuming the  $[\text{N II}]\lambda 6583$  line (less affected by DIG contribution, e.g., Blanc et al. 2009) instead of  $[\text{S II}]$ , leads to infer lower  $T_{\text{eff}}$  value for the considered objects.

We assumed that a model successfully represents an object if it reproduces the intensities of emission lines within an uncertainty lower than  $\pm 25$  per cent. If no model was able to satisfy this criterion

considering the  $N_e$  value defined as described above, a new series of models varying  $N_e$  were built. For 13 (over the 24) objects with  $N_e$  derived from their observed spectra (using IRAF) we have to run models varying  $N_e$  to fit the observed intensities ratios. These objects are highlighted with the superscript "(a)" in Table 2. This methodology is similar to that used by Dors et al. (2017) to derive the nitrogen and oxygen abundances for a sample of Seyfert 2 objects.

The PHYMIR optimization method (van Hoof 1997), implemented into the CLOUDY code (Ferland et al. 2017), was applied to vary the nebular parameters and select the best model. In Table 1 the model-predicted emission-line intensities ratios for each object of the sample are listed, while the resulting final model parameters are listed in Table 2. The atmosphere models of Rauch (2003) are defined for  $T_{\text{eff}}$  values between 50 and 190 kK with a step of 10 kK. Thus, the  $T_{\text{eff}}$  values derived for our sample are the ones interpolated between the Rauch (2003) available values.

To obtain the uncertainty in our abundance estimations, we consider as benchmarks three models with metallicities ( $Z/Z_{\odot}$ ) = 2.2, 1.0 and 0.2, which represent the range and the mean value derived for the objects in our sample (see Sect. 4). The  $T_{\text{eff}}$ ,  $N_e$  and  $\log U$  parameters were assumed to be 115 000 K,  $400 \text{ cm}^{-3}$  and  $-3.5$ , respectively, about the average values obtained from our model fitting to the observational data (see Table 2). Taking into account these model parameters, a series of models varying separately the O/H and N/H abundances by a factor of  $\pm 0.3$  dex (step of 0.1 dex) were built. Thus, the uncertainty in our fitting was obtained considering the abundance range, adopted in the models, where the emission line intensities differ by  $\pm 25$  percent from the originally anticipated values (see also Dors et al. 2017). We found that variations of about  $\pm 0.2$  dex and  $\pm 0.1$  dex in O/H and N/H abundances,

<sup>2</sup> [http://web.physics.ucsb.edu/~phys233/w2014/hazy1\\_c13.pdf](http://web.physics.ucsb.edu/~phys233/w2014/hazy1_c13.pdf)

<sup>3</sup> <http://www.iaa.csic.es/~epm/HII-CHI-mistry.html>

**Table 2.** Assumed model parameter values used to fit the emission lines observed of our LINER sample.

Plate-IFU	log(O/H)	log(N/H)	$T_{\text{eff}}$ (K)	log $U$	$N_e$ ( $\text{cm}^{-3}$ )
7495-12704	-3.01	-3.43	85186	-3.20	121
7977-3704	-3.67	-4.36	119218	-3.63	1615
7977-12703	-3.68	-4.36	85852	-3.63	2793 <sup>(a)</sup>
7990-12704	-3.09	-3.82	85187	-3.45	843 <sup>(a)</sup>
8083-12704	-3.10	-3.66	80954	-3.36	41 <sup>(a)</sup>
8140-12703	-2.97	-3.98	147970	-3.76	1261 <sup>(a)</sup>
8247-3701	-3.05	-3.73	71565	-3.48	1025
8249-12704	-3.04	-3.69	92854	-3.20	454 <sup>(a)</sup>
8254-3704	-3.09	-3.87	95126	-3.55	1100 <sup>(a)</sup>
8257-1902	-3.83	-4.33	92931	-3.56	675 <sup>(a)</sup>
8259-9102	-3.28	-4.09	101921	-3.55	272 <sup>(a)</sup>
8313-9102	-3.19	-3.74	85510	-3.46	834 <sup>(a)</sup>
8313-12705	-3.18	-3.78	108132	-3.37	181
8318-12703	-3.04	-3.69	100000	-3.48	833
8320-9102	-3.04	-3.69	84341	-3.40	1097
8330-9102	-3.06	-3.50	87876	-3.26	83
8332-6103	-3.19	-4.02	119486	-3.49	1384 <sup>(a)</sup>
8440-12704	-3.00	-3.72	104736	-3.53	331
8481-1902	-3.11	-3.98	98296	-3.57	1077
8482-12703	-3.07	-3.84	150321	-3.55	1191
8550-6103	-3.78	-4.25	99555	-3.55	599 <sup>(a)</sup>
8550-12705	-3.22	-4.11	150761	-3.58	1843
8552-9101	-3.07	-3.81	124483	-3.66	173
8601-12705	-3.94	-4.37	109605	-3.51	382
8588-9101	-3.91	-4.34	88103	-3.55	14
8138-9101	-3.02	-3.88	103309	-3.55	561
8482-9101	-3.28	-3.86	108303	-3.24	516
8554-1902	-3.53	-4.07	65942	-3.25	1163
8603-12703	-3.04	-3.63	71404	-3.32	134
8604-6102	-3.14	-3.80	95684	-3.43	734
8606-3702	-3.01	-3.90	141758	-3.52	1415
7990-6103	-3.47	-4.35	161338	-3.60	89 <sup>(a)</sup>
8243-9102	-3.33	-3.91	155345	-3.61	1463
8243-12701	-3.13	-4.00	154776	-3.55	593 <sup>(a)</sup>
8332-12705	-3.23	-4.06	189387	-3.52	189
8549-3703	-3.26	-4.13	189160	-3.48	191
8550-12704	-3.39	-4.04	149596	-3.59	239
8138-3702	-2.96	-4.01	188397	-3.59	1248
8482-3704	-3.35	-4.09	121998	-3.63	103
8604-12703	-3.30	-3.97	167932	-3.46	363

(a) Objects for which we needed to build photoionization models assuming as input  $N_e$  values differ from those derived from observational [S II] $\lambda 6716/\lambda 6731$  line ratio, as described in Sect. 3.2.

respectively, produce variations of about  $\pm 25$  per cent in the intensities of the [O II] $\lambda 3727/H\beta$ , [O III] $\lambda 5007/H\beta$ , [N II] $\lambda 6584/H\beta$ , and [S II] $(\lambda 6716 + \lambda 6731)/H\beta$  emission line ratios considered.

Since the PHYMIR method implemented in the CLOUDY (Ferland et al. 2017) code does not produce error estimates in the nebular parameters, these values are considered uncertainties in our O/H ( $\pm 0.2$  dex) and N/H ( $\pm 0.1$  dex) abundance estimations.

## 4 RESULTS AND DISCUSSIONS

We were able to obtain detailed photoionization models for 40 galaxies from our original sample of 43 objects. The cause of the model's failure in 3/43 LINER models was the difficulty in reproducing both high observational [O II]/ $H\beta$  and [O III]/ $H\beta$  values, i.e. values higher than  $\sim 15$ . These objects (not listed in Table 1)

are 8131-9102, 8252-12702 and 8258-12704 and they are represented in Fig. 1 by blue points. Possibly, for these three LINERs, the ionizing source is hotter than the upper limit of 190 kK of the Rauch (2003) atmosphere models, e.g., accreting, nuclear-burning white dwarfs (WDs) with photospheric temperatures of  $10^5$ - $10^6$  K (Woods & Gilfanov 2013). However, Johansson et al. (2016) argued that the ionizing source in RGs is mainly composed of pAGB stars rather than accreting, nuclear-burning WDs.

Fig. 2, bottom panels, shows the intensities of observational emission-line ratios ( $x$ -axis) compared with those predicted by the photoionization models ( $y$ -axis). In the upper part of each panel of this figure, the ratios between the observed and predicted intensities versus the observed ones are shown. It can be noted a very good agreement between the predicted and observational emission line ratios.

### 4.1 Implications of model assumptions

Before analyzing the results, we discuss some implications of our model assumptions on the N and O abundance estimates.

#### 4.1.1 Electron density variation

Spatially resolved observational studies have found that  $N_e$  varies along the nebular radius, in the sense that near the ionizing source higher values are derived in comparison to those in the outskirt gas regions. For instance, in their pioneering study, Osterbrock & Flather (1959) found, based on the [O II] $\lambda 3716/\lambda 3729$  line ratio, a steep radial density gradient in the Orion Nebula, with  $N_e$  decreasing from  $\sim 10^4 \text{ cm}^{-3}$  in the centre to  $\sim 10^2 \text{ cm}^{-3}$  near the edge. Additional studies have confirmed the existence of radial profiles or variations of  $N_e$  in SF regions (e.g., Castaneda et al. 1992; Copetti et al. 2000; Mesa-Delgado & Esteban 2010; Mesa-Delgado et al. 2011; Cedrés et al. 2013; O'Dell et al. 2017) and AGNs (e.g., Congiu et al. 2017; Freitas et al. 2018; Kakkad et al. 2018; Mingozi et al. 2019). Moreover,  $N_e$  estimation based on lines emitted by ions with higher ionization potential than  $S^+$ , such as [Ar IV] and [Fe III] emission-lines, which trace the density in the inner gas layers, have revealed that  $N_e$  in SF regions (e.g., Mesa-Delgado et al. 2011) and AGNs (e.g., Congiu et al. 2017) can reach values in order of  $20\,000 \text{ cm}^{-3}$ . Such high  $N_e$  values can produce a suppression of some forbidden emissions lines and a wrong interpretation from photoionization models, hence the density assumed in our models is derived from the observational [S II] lines ratio, which could not be a representative value for the entire gas. Moreover, our analysis considers integrated spectra of the nuclear zones of the galaxies, therefore, the electron density values obtained in the present work must be considered as mean values.

To investigate the  $N_e$  influence on our abundance estimations, we carried out some simulations. Firstly, we considered the representative model for the 8588-9101 object as a benchmark, hence it presents the lowest derived  $N_e$  value ( $14 \text{ cm}^{-3}$ ; see Table 2). Thus, we carried out a new fitting to the observational line intensities ratios of this object (see Table 1) assuming six fixed values of  $N_e$ : 1 000, 2 000, 3 000, 4 000, 5 000 and 10 000  $\text{cm}^{-3}$ . After running these models, we did not observe any abundances variation for models with  $N_e = 1\,000, 2\,000, 3\,000$  and  $4\,000$ , while for the photoionization model with  $N_e = 5\,000 \text{ cm}^{-3}$  we found a discrepancy of approximately 0.15 dex for O/H and around 0.03 dex for N/H when comparing with the benchmark model results. We did not find a solution for the model with  $N_e = 10\,000 \text{ cm}^{-3}$  because

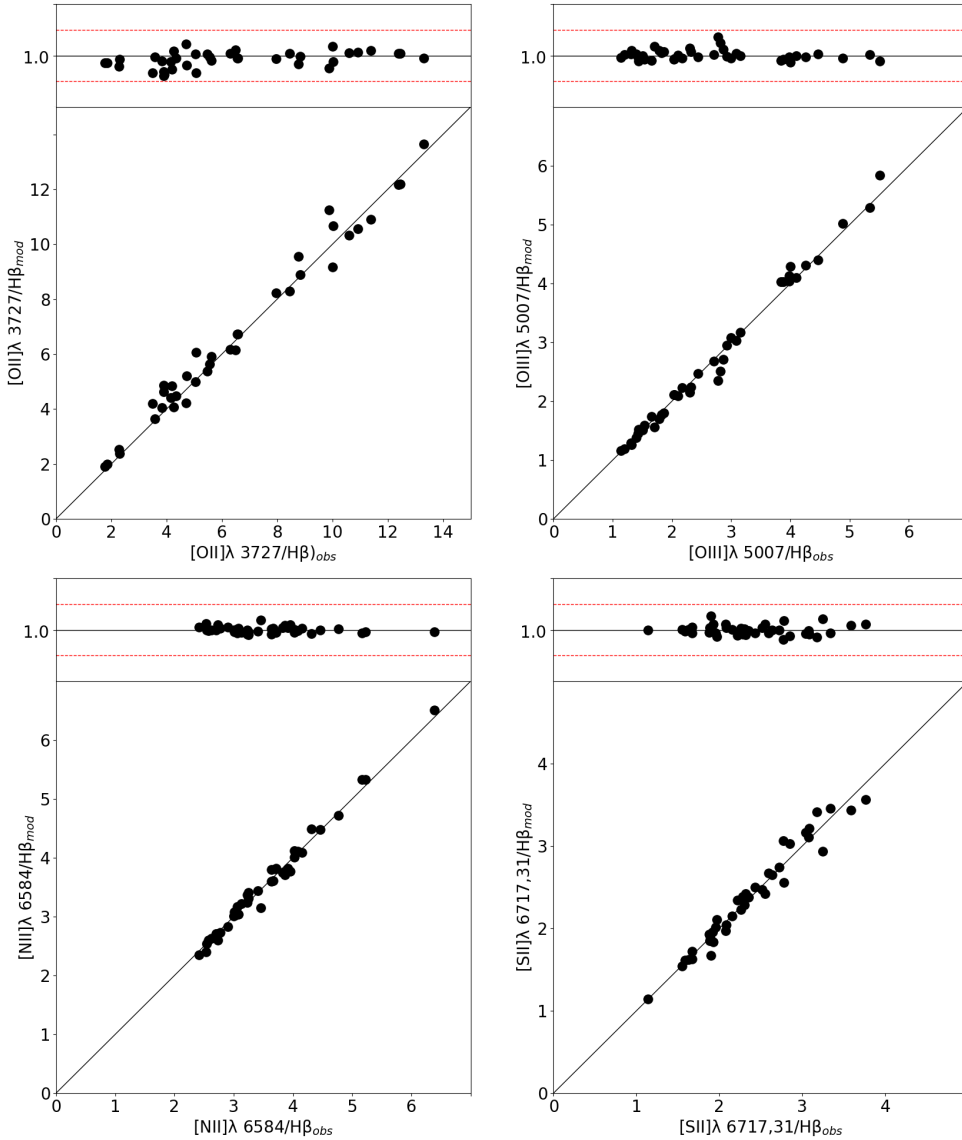


**Figure 2.** Bottom part of each panel: comparison between model predictions (y-axis) and observed (x-axis) emission line ratios (normalized by  $H\beta$ ) for our LINER sample. The solid line represents the equality of the two estimates. Top part of each panel: the ratio between the observed and predicted intensities versus the observed emission line intensities ratios. The red dashed lines represent the adopted limit of  $\pm 25\%$  between the observed and predicted line ratios to consider that a model successfully represents an object.

it underpredicts the  $[O\text{II}]\lambda 3727/H\beta$  in comparison to the observational value, possibly due to effects of collisional deexcitation (not present in the 8588-9101 object) in which produce a suppression in the emission of collisionally excited lines. The critical density for the  $[O\text{II}]\lambda 3726$  and  $\lambda 3729$  lines is in order of  $10^3\text{ cm}^{-3}$  (see e.g., Dors et al. 2023).

Secondly, we assumed a density profile for the gas. For instance, Revalski et al. (2018a) found for the AGN in Mrk 573 a peak of about  $N_e = 3000\text{ cm}^{-3}$  at the center and a decrease following a shallow power law with the radial distance ( $r$ ):  $N_e \sim r^\alpha$ , being  $\alpha = -0.5$ . The power law derived by these authors includes only points inner  $\sim 1.7$  arcsec ( $\sim 600$  pc) of radius (see also Revalski et al. 2018b, 2021; Ruschel-Dutra et al. 2021). Regarding LINERs, it seems that such density profile found for SF regions and AGNs is also present. In fact, Constantin et al. (2015) presented an analysis

of optical emission-line intensities, obtained by ground-based and Hubble Space Telescope spectroscopy, of a sample of  $\sim 100$  nearby galaxy nuclei, including LINERs. These authors found, for all types of nuclei, indications that gas densities are generally higher in the most central regions. To analyze the effect of density profile on our abundance estimates, we choose as a benchmark the model representing the 7977-12703 galaxy, hence the highest density value ( $N_e = 2793\text{ cm}^{-3}$ , see Table 2) was derived for this object. We assumed  $\alpha = -2.0, -1.0, -0.5,$  and  $-0.1$  and carried out new fitting to the observational line ratio intensities of this object. We found that models assuming radial density profiles result in very similar line intensity ratio (less than 10%) as those predicted by the constant density model and, consequently, the same nebular parameters as those for the constant density model ( $N_e = 2793\text{ cm}^{-3}$ ). The same

result was found by [Dors et al. \(2018\)](#), who used photoionization model simulations of narrow-line regions of AGNs.

Therefore, we can assume that the uncertainties due to high and constant electron density values for our O/H and N/H estimates are  $\sim 0.15$  and  $\sim 0.03$  dex, respectively. Also, we conclude that density variation along the nebular radius does not influence our abundance estimates (see also [Dors et al. 2020](#); [Armah et al. 2023](#)).

#### 4.1.2 Dust content

The abundance of elements (e.g. Fe, Mg, Si, etc.) contained in dust grains in the gas phase of gaseous nebulae is poorly known due to the difficulty of estimating it (see e.g., [Sofia et al. 1994](#); [Garnett et al. 1995](#); [Brinchmann et al. 2013](#); [Martín-Doménech et al. 2016](#); [Konstantopoulou et al. 2023](#)). Interstellar dust grains absorb and scatter the ionizing radiation, decreasing the hardness of the radiation field and thus influencing the temperature and ionization structures of the gas ([Maciel & Pottasch 1982](#); [Charlot & Longhetti 2001](#); [Groves et al. 2004](#); [Feltre et al. 2016](#)). Also, some fraction of oxygen<sup>4</sup> (about  $\sim 0.1$  dex) is expected to be locked into dust grains (see e.g., [Esteban et al. 1998](#); [Meyer et al. 1998](#); [Peimbert & Peimbert 2010](#)). Thus, any oxygen abundance estimates of the gas phase in gaseous nebulae trend to underestimate the abundance of this element if a correct depletion is not taken into account (see e.g., [Pilyugin et al. 2007](#)).

Our models are dust free, thus, we built another model simulation using `CLOUDY` code ([Ferland et al. 2017](#)) taking into account the dust present in the gas phase to analyze the possible effect on our abundance estimates. Since the dust abundance seems to be correlated with the gas phase metallicity ([Peimbert & Peimbert 2010](#)), we consider as benchmarks three models with the highest, intermediate, and lowest metallicity derived from our simulations, i.e. the models representing the 8138-3702 [(Z/Z<sub>⊙</sub>) = 2.2], 8549-3703 [(Z/Z<sub>⊙</sub>) = 1.0] and 8601-12705 [(Z/Z<sub>⊙</sub>) = 0.2] objects, respectively (see Table 2). Following [Dors et al. \(2011\)](#), the grain abundances ([van Hoof et al. 2001](#)) were linearly scaled with the metallicity. To take the depletion of refractory elements onto dust grains into account, the abundance of the elements Mg, Al, Ca, Fe, Ni, and Na were reduced by a factor of 10, and Si by a factor of 2 ([Garnett et al. 1995](#)), relative to the adopted metallicity in each model. The dusty models were fitted to the corresponding observational data of each object and the resulting abundances were compared with those predicted by the dust-free models. From these simulations, we found that O/H abundances predicted by dusty models are lower by a factor of 0.20, 0.10, and 0.05 dex for the models with the highest, intermediate, and lowest metallicity, respectively, in comparison to predictions by dust-free models. The nitrogen abundances did not change taking into account the dust presence in the models.

We define the uncertainty in O/H abundances due to the dust present in our objects as being 0.12 dex, the mean value of the discrepancy derived above.

## 4.2 N and O abundances

The methodology presented by [Peimbert & Costero \(1969\)](#) to calculate electron temperatures and elemental abundances of gaseous nebulae opened a new window in astronomy (see also [Seaton 1960](#); [Aller & Liller 1968](#); [Osterbrock 1970, 1974](#)), in the sense that it

enabled the knowledge of the chemical abundances in galaxies relying on a (relatively) precise method, i.e. the  $T_e$ -method (see e.g., [Pilyugin 2003](#); [Hägele et al. 2006, 2008](#); [Toribio San Cipriano et al. 2017](#)). Over decades, the use of the  $T_e$ -method has permitted to calculate heavy elemental abundances (e.g., O, N, S) in nearby galaxies (e.g., [Peimbert 1975](#); [Talent & Dufour 1979](#); [Rayo et al. 1982](#); [Fierro et al. 1986](#); [van Zee et al. 1998](#); [Izotov & Thuan 1999](#); [Kennicutt et al. 2003](#); [Hägele et al. 2011, 2012](#); [Berg et al. 2015](#); [Rogers et al. 2022](#)) and, recently, in the early universe (see e.g. [Arellano-Córdova et al. 2022](#); [Sanders et al. 2023](#); [Curti et al. 2023](#)).

Due to the difficulty of using this method, i.e. the need to measure weak auroral emission lines such as [O III]λ4363, made it necessary to develop strong-line methods. The method proposed by [Pagel et al. \(1979\)](#) permits to estimate the O/H abundance measuring only the  $R_{23} = ([\text{O II}]\lambda 3727 + [\text{O III}]\lambda 4959 + \lambda 5007) / \text{H}\beta$  strong lines ratio. Further authors have adapted this method to estimate the relative abundances of other elements. For instance, [Pérez-Montero & Díaz \(2005\)](#) proposed a calibration between the strong  $N2O2 = [\text{N II}]\lambda 6584 / [\text{O II}]\lambda 3727$  lines ratio and the N/O abundance for SF regions. Unfortunately, most studies have predominantly concentrated on developing strong-line methods to estimate ionized gas content in SF regions, while AGNs and LINERs are rarely analyzed due to their poorly understood ionization mechanisms, particularly in the case of LINERs. Thus, there have been few studies estimating gas-phase abundances in regions with ionization similar to AGNs and LINERs, such as [Kumari et al. \(2019\)](#), [do Nascimento et al. \(2022\)](#) and [Metha et al. \(2022\)](#).

Recently, [Oliveira et al. \(2022\)](#) proposed the first (semi-empirical) calibration for LINERs between strong emission lines and the O/H abundance. These authors were able to estimate the abundances for 43 LINERs, possibly ionized by pAGB stars, finding values in the range of  $8.5 \lesssim 12 + \log(\text{O}/\text{H}) \lesssim 8.8$ , or  $0.60 \lesssim (Z/Z_{\odot}) \lesssim 1.40$ . [Pérez-Díaz et al. \(2021\)](#) compiled optical spectroscopic data of a sample of 40 LINERs from the Palomar Survey ([Ho et al. 1995, 1997](#)) and 25 observed by [Pović et al. \(2016\)](#) at the Calar Alto Observatory, and applied the `HI-CHI-MISTRY` code ([Pérez-Montero 2014](#), hereafter `HCM` code) to derive O/H and N/O. This code establishes a Bayesian-like comparison between the predictions from a grid of photoionization models built with the `CLOUDY` code ([Ferland et al. 2017](#)) covering a large range of input parameters and using the lines emitted by the ionized gas. These authors found a range of  $8.0 \lesssim 12 + \log(\text{O}/\text{H}) \lesssim 8.9$  (with a median value of  $\sim 8.6$  dex) and  $-0.2 \lesssim \log(\text{N}/\text{O}) \lesssim -1.1$  (with a median value of  $\sim -0.6$ ) for their LINERs sample. The nitrogen abundance estimates by [Pérez-Díaz et al. \(2021\)](#) seem to be the first estimation in LINERs. In particular, the N/O abundance ratio is a useful tool to study the interplay of galactic processes, for instance, star formation efficiency, the timescale of infall, and outflow (e.g., [Johnson et al. 2023](#); [Magrini et al. 2018](#)) as well as it can be used as a metallicity indicator (e.g., [Pérez-Montero & Contini 2009](#)).

As indicated by the WHAN diagram (see Fig. 1), the LINERs sample selected for the present work has pAGB stars as the main ionization source, allowing to apply of the  $T_e$ -method and/or standard photoionization models to obtain elemental abundances. However, for our LINERs sample, auroral lines were not measured and it was only possible to estimate both O and N abundances through detailed photoionization models. This technique has also been employed in SF regions (e.g., [Dors & Copetti 2006](#); [Pérez-Montero et al. 2010](#)) and AGNs (e.g., [Dors et al. 2017, 2021](#); [Contini 2017](#)) studies and trends to overestimate elemental abundances by 0.1-0.2 dex in comparison to those through the  $T_e$ -method (e.g., [Pérez-Montero 2014](#); [Dors et al. 2020](#)). The source of this discrepancy

<sup>4</sup> For a review on dust abundance see [Jenkins \(1987, 1989\)](#).

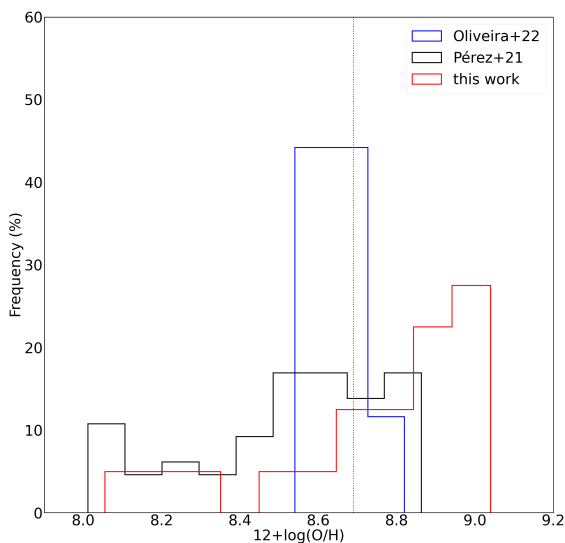


**Figure 3.** Histograms comparing O/H estimations derived by Oliveira et al. (2022), as well as the estimations derived by Pérez-Díaz et al. (2021) and O/H values derived through our detailed models. The dashed vertical line represents the solar abundance  $12 + \log(\text{O}/\text{H})_{\odot} = 8.69$ , taken from Allende Prieto et al. (2001).

is an open problem in astronomy and it is been attributed to the presence of electron temperature fluctuations in gaseous nebulae (Peimbert 1967) and AGNs (Riffel et al. 2021), departure from Maxwell–Boltzmann equilibrium energy distribution (Binette et al. 2012; Nicholls et al. 2012) or a simplified geometry (e.g., Jin et al. 2022) assumed in photoionization models. However, the scenarios listed above do not provide a plausible explanation for this discrepancy problem. It is beyond the goal of this paper to address this issue and we only emphasize that our theoretical abundances can be possibly overestimated by 0.1–0.2 dex in comparison to those via the  $T_e$ -method.

Regarding the range of the derived oxygen abundances, we found a distribution ranging from  $8.0 \lesssim 12 + \log(\text{O}/\text{H}) \lesssim 9.0$  [ $0.20 \lesssim (Z/Z_{\odot}) \lesssim 2.0$ ], with a mean value of  $\langle 12 + \log(\text{O}/\text{H}) \rangle = 8.83 \pm 0.27$ . In Fig. 3, we show a histogram of the computed oxygen abundance distribution. Notably,  $\sim 72\%$  of the objects in our study present values higher than the solar abundance. The resulting O/H range is wider than that found by Oliveira et al. (2022),  $-8.5 \lesssim 12 + \log(\text{O}/\text{H}) \lesssim 8.8$  or  $0.6 \lesssim (Z/Z_{\odot}) \lesssim 1.4$  (blue histogram in Fig. 3), obtained from a semi-empirical calibration, and assuming a fixed of (N/O)–(O/H) abundance relation taken from Carvalho et al. (2020). On the other hand, the found range is consistent with that derived by Pérez-Díaz et al. (2021) (black histogram in Fig. 3), relying on the HCM code, taking into account the uncertainty in the O/H estimations via the present method ( $\sim 0.2$  dex).

We found that our LINERs sample shows a range of  $7.6 \lesssim 12 + \log(\text{N}/\text{H}) \lesssim 8.5$  or  $0.4 \lesssim (\text{N}/\text{N}_{\odot}) \lesssim 3.7$ . The mean value is  $\langle 12 + \log(\text{N}/\text{H}) \rangle = 8.05 \pm 0.25$  or  $\langle (\text{N}/\text{N}_{\odot}) \rangle = 1.6$ , having oversolar values in about 70 per cent of the objects. The nitrogen abundance range derived via the HCM code by Pérez-Díaz et al. (2021) is

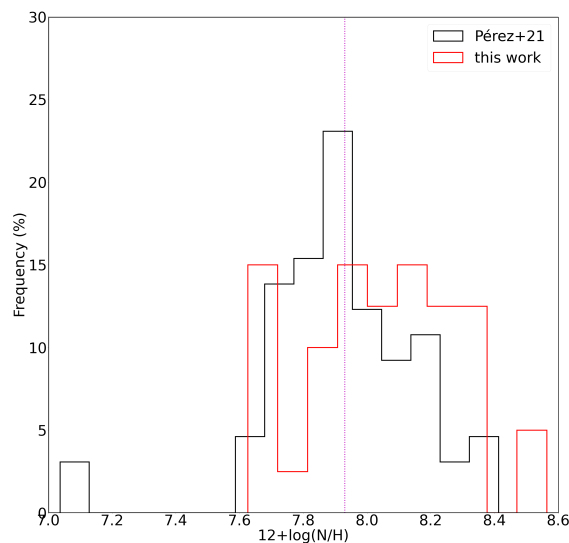


**Figure 4.** Histograms comparing N/H estimations derived by Pérez-Díaz et al. (2021) and N/H values derived through our detailed models. The dashed vertical line represents the solar abundance  $12 + \log(\text{N}/\text{H})_{\odot} = 7.93$ , taken from Holweber (2001).

$7.04 \lesssim 12 + \log(\text{N}/\text{H}) \lesssim 8.4$  [ $0.1 \lesssim (\text{N}/\text{N}_{\odot}) \lesssim 3.0$ ], in agreement with our results, as shown in Fig. 4. However, the mean value derived by Pérez-Díaz et al. (2021) is  $\langle 12 + \log(\text{N}/\text{H}) \rangle = 7.93 \pm 0.24$  [ $\langle (\text{N}/\text{N}_{\odot}) \rangle \sim 1.0$ ], a factor of  $\sim 0.1$  dex lower than the mean value obtained for our sample. The reason for this discrepancy is due to three outlier objects of the Pérez-Díaz et al. (2021) sample present very low ( $12 + \log(\text{N}/\text{H}) \lesssim 7.10$ ) nitrogen abundances.

To explore a possible correlation between nitrogen and oxygen abundances, we plot in Fig. 5 the  $\log(\text{N}/\text{O})$  versus  $12 + \log(\text{O}/\text{H})$  estimations for the objects in our sample. In this figure, we also included:

- (i) Estimates for 65 LINERs compiled from the dataset presented in Pérez-Díaz et al. (2021). These authors determined the abundances using the HCM code for a sample of 40 LINERs in the local universe and taken from the Palomar Survey (Ho et al. 1995, 1997). Additionally, they compared their results with a sample of 25 more distant LINERs at  $z = 0.04 - 0.11$  observed by Pović et al. (2016) at the Calar Alto Observatory.
- (ii) Abundance values of 176 disk H II regions located in four local spiral galaxies derived using the  $T_e$ -method by Berg et al. (2020) and resulting from the CHAOS project<sup>5</sup>.
- (iii) Estimates for 44 Seyfert 2 nuclei ( $z < 0.1$ ) derived by Dors et al. (2017) through detailed photoionization modeling.
- (iv) Nuclear abundance values of 1431 spiral galaxies obtained extrapolating their disk metallicity gradients derived by Zinchenko et al. (2021), by applying the R calibration (Pilyugin & Grebel 2016), observed by the MaNGA survey.
- (v) Direct  $T_e$  estimates for 4 H II belonging to the dwarf blue compact galaxy NGC 4640 derived by Kumari et al. (2018).

<sup>5</sup> <https://www.danieleleberg.com/chaos> (Berg et al. 2015)

(vi) Estimates for 2 H II regions of the dwarf irregular galaxy NGC 4163 by Zinchenko & Pilyugin (2022).

(vii) Estimations for H II regions derived by Pilyugin & Grebel (2016) using the C method (Pilyugin et al. 2012). These objects reach lower oxygen abundance values showing the change between the primary and secondary nitrogen production behaviour (see also Dors et al. 2017).

(viii) The primary (red dashed line) and secondary production (black dashed line) lines, as proposed by Belfiore et al. (2015). In regions with low metallicities, i.e.  $12 + \log(\text{O}/\text{H}) < 8.35$ , nitrogen is considered as a primary nucleosynthetic product, showcasing a flat behaviour with  $\log(\text{N}/\text{O}) \sim -1.5$ . Conversely, for regions with  $12 + \log(\text{O}/\text{H}) > 8.35$ , nitrogen takes on the role of a secondary nucleosynthetic product. In this context, a relationship between N/O and O/H is expressed as  $\log(\text{N}/\text{O}) = 4.0 \times [12 + \log(\text{O}/\text{H})] - 8.7$ , as derived by Belfiore et al. (2015) using data obtained through the Sloan DR7.

In Fig. 5, we can note that LINERs present similar N/O and O/H abundances to those derived for Seyfert 2 nuclei, indicating that these distinct object classes have similar ISM enrichment. Moreover, LINERs estimates occupy a region similar to the most metallic and innermost disk H II regions. This is an expected result because most parts of spiral galaxies exhibit negative radial abundance gradients, with the highest abundances derived at the lowest galactocentric distances (see e.g., van Zee et al. 1998; Kennicutt et al. 2003; Pilyugin et al. 2004; Dors & Copetti 2005; Rogers et al. 2022; do Nascimento et al. 2022). In Table 3, the statistics of the estimates shown in Fig. 5 are presented. As can also be seen in Fig. 5, our LINERs estimates are located toward the higher N/O regions, having an orthogonal distribution (with a correlation coefficient of  $r = -0.45$ ) with respect to the values predicted by the line representing the secondary production of nitrogen. In our sample, LINERs with the highest O/H values present the lowest N/O ratios, which are, in turn, lower than those expected from the theoretical secondary curve and H II region observations. It could be indicating that our LINERs present mainly a secondary nitrogen production together with different mechanisms producing the observed offset, as we will discuss in what follows.

We can also note in Fig. 5 that a distinct (N/O)-(O/H) relation for LINERs in comparison to those for other object classes is observed. To confirm that, we consider the abundance estimates in Fig. 5 and conducted a linear fitting analysis (not shown) to the abundance estimates of the samples, except for the sample of SF galaxies by Zinchenko et al. (2021). For this specific SF galaxy sample, we employed a quadratic equation for the fitting process. The fitted equations and the Pearson correlation coefficient ( $r$ ) values are listed in Table 3. As can be seen, a positive correlation between  $\log(\text{N}/\text{O})$  and  $12 + \log(\text{O}/\text{H})$  is clearly found for the SF galaxy samples from Zinchenko et al. (2021) and Berg et al. (2020). In contrast, no significant correlation between N/O and  $12 + \log(\text{O}/\text{H})$  was found for the sample of Seyfert nuclei from Dors et al. (2017). On the other hand, a negative correlation with  $r = -0.45$  was derived for the LINERs in our sample, and with  $r = -0.42$  when we combined the two samples compiled by Pérez-Díaz et al. (2021) [see item (i) in Section 4.2]. It worth to be mentioned that if only the sample of 45 LINERs at the local universe listed by Pérez-Díaz et al. (2021) is considered, no correlation is found. The unexpected N/O negative trend was also reported by Kumari et al. (2018) for the blue compact dwarf galaxy NGC 4670 (and some other dwarf galaxies) as well as by Zinchenko & Pilyugin (2022) for the dwarf irregular galaxy NGC 4163. Both galaxies were also studied per-

forming a spatially-resolved analysis. It is important to emphasize that negative gradients found for these two dwarf galaxies were derived for objects showing significantly lower N/O and  $12 + \log(\text{O}/\text{H})$  values (which seems to be located close to the primary nitrogen production zone or in a transition zone where both mechanisms of nitrogen production could be of similar importance; see Fig. 5) than the results obtained for the LINERs studied in the present work. As mentioned by Kumari et al. (2018), the negative trend of N/O could be explained by various mechanisms, such as outflows, star formation efficiency (SFE), and Wolf-Rayet (WR) stars, which are briefly discussed below.

To investigate the presence of outflows in our LINERs, we followed the approach by Ilha et al. (2019). These authors explored the impact of AGNs on the kinematics of their host galaxies, analyzing a sample with 62 AGNs and 109 inactive galaxies. They derived the fractional velocity dispersion differences between gas and stars [ $\sigma_{\text{frac}} = (\sigma_{\text{gas}} - \sigma_{\text{stars}})/\sigma_{\text{stars}}$ ]. A higher value of  $\sigma_{\text{frac}}$  indicates disturbed kinematics, likely due to outflows. Ilha et al. (2019) found that 75% of their AGNs have values of  $\sigma_{\text{frac}} > -0.13$ , while 75% of inactive galaxies have  $\sigma_{\text{frac}} < -0.04$ . We computed  $\sigma_{\text{frac}}$  for our sample of LINERs and found that 55% of it has  $\sigma_{\text{frac}} > -0.04$ . However, these higher values of  $\sigma_{\text{frac}}$  are not associated with higher values of N/O (see Fig. 6, left panel) and we can not conclude that outflows are responsible for the negative trend on N/O. About the SFE, Kumari et al. (2018) mentioned that, in the case of NGC 4670, spaxels with higher N/O ratios and lower metallicities show higher H $\alpha$  fluxes, suggesting a connection between the N/O ratio and a very recent enhancement of the star formation rate. However, we did not find such a correlation for our LINERs (see right panel of Fig. 6), likewise Zinchenko & Pilyugin (2022) did not find this correlation for NGC 4163. Finally, regarding the presence of WR stars, two important broad features in the optical spectra can reveal the presence of this kind of stars (see e.g. López-Sánchez & Esteban 2008): the so-called blue WR bump (mainly formed by N V, N III, C III + C IV and He II $\lambda$ 4686 emission lines) and the red WR bump (formed by the C v emission lines). A visual inspection of our datacubes did not reveal any significant traces of these WR features. Therefore, the mechanisms highlighted by Kumari et al. (2018) can not explain the negative trend in the N/O ratios observed in the present study.

In a recent work, Zinchenko (2023) found a significant scatter around the usual O/H-N/O curve in counter-rotating gas located in the central parts of galaxies. He suggested that such gas most likely fall onto these galaxies from areas outside their disks. We searched for hints of co-rotation in the velocity maps of the LINERs in our sample and we did not find any evidence of this phenomenon.

We also investigated the correlation between the N/O abundances and the stellar masses of the host galaxies. The stellar masses of the hosting galaxies are in the range of  $10 \lesssim \log(M_*/M_\odot) \lesssim 11.2$  and were taken from the MaNGA catalog Pipe3D<sup>6</sup> (Sánchez et al. 2016). As is shown in Fig. 7, a large scatter was found and no correlation between these parameters is observed. A similar result was obtained by Pérez-Díaz et al. (2021) finding a very small Pearson's correlation coefficient ( $r = 0.038$ ) for their sample. It is important to note that our sample is composed only by massive galaxies, which occupy the flattened part of the Mass-Metallicity relation (MZR) curve, i.e., the region where no significant variation of metallicity ( $\sim 0.1$  dex) with the mass is found (see also Thomas et al. 2019). Likewise, as reported by Pérez-Díaz et al. (2021), for SF galaxies there is a relation between N/O and stellar masses in the

<sup>6</sup> [https://data.sdss.org/datamodel/files/MANGA\\_PIPE3D](https://data.sdss.org/datamodel/files/MANGA_PIPE3D)

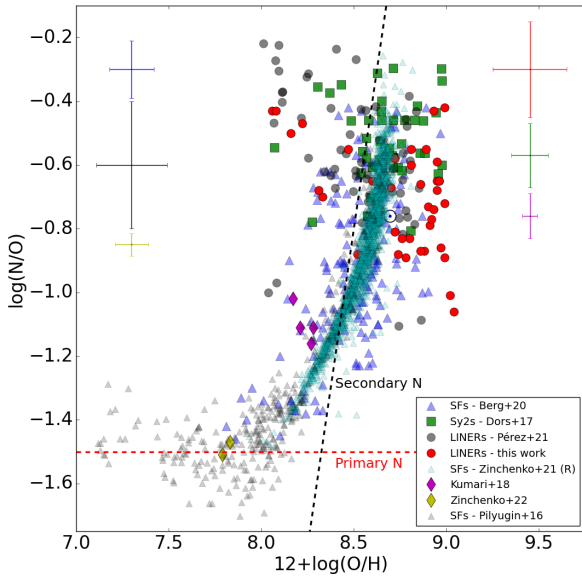


**Figure 5.**  $\log(N/O)$  vs.  $12+\log(O/H)$ . Red points are the predicted values for our LINERs sample. Blue triangles are the values estimated by Berg et al. (2020) for disk H II regions. Green squares are the values derived by Dors et al. (2017) for Seyfert 2 nuclei, while grey points are the abundances reported by Pérez-Díaz et al. (2021) for 65 LINERs. Cyan triangles are values derived applying the R calibration (Pilyugin & Grebel 2016) to 1431 SF galaxies as reported by Zinchenko et al. (2021). Purple diamonds are the Kumari et al. (2018) data, and yellow diamonds are the Zinchenko & Pilyugin (2022) ones. Grey triangles are the SFs sample by Pilyugin & Grebel (2016). The solar values taken from Holweger (2001) and Grevesse & Sauval (1998) are also included in the plot with the solar symbol. The red and black dashed lines are taken from Belfiore et al. (2015) and represent the expected N/O when nitrogen is mainly due to a primary production and a linear fit to the N/O distribution of galaxies in SDSS DR7 with  $12+\log(O/H) > 8.3$  (secondary nitrogen production), respectively. Error bars represent the average uncertainties in O/H and N/O estimations.

$7 \lesssim \log(M_*/M_\odot) \lesssim 11$  range. On the other hand, these authors neither find any relation between N/O and stellar masses for AGN galaxies, i.e., Seyfert and LINER galaxies hosted in more massive galaxies ( $9 \lesssim \log(M_*/M_\odot) \lesssim 11$ ).

## 5 CONCLUSION

Using optical data from 40 LINER galaxies taken from the MaNGA survey and classified as retired galaxies in the WHAN diagnostic diagram, we built detailed photoionization models using the CLOUDY code to reproduce optical emission line intensities ratios of these objects. Based on these models we were able to estimate the oxygen and nitrogen abundances of the galaxies in our sample. We found that our LINER objects have oxygen and nitrogen abundances in the ranges of  $8.0 \lesssim 12+\log(O/H) \lesssim 9.0$  and  $7.6 \lesssim 12+\log(N/H) \lesssim 8.5$ , with mean values of  $8.74 \pm 0.27$  and  $8.05 \pm 0.25$ , respectively. We also found that about 70% of the objects in our sample have oversolar oxygen and nitrogen abundances. The O/H and N/O abundance of our sample are in consonance with those obtained for Seyfert 2 nuclei as well as for the most metallic H II regions located in spiral galaxies. We compared our results with the ones obtained for another

LINERs sample whose estimates were taken from the literature. We found a very good agreement between each other. The LINERs belonging to our sample are located in the higher N/O region of the O/H-N/O diagram presenting a negative correlation between these two parameters with a correlation coefficient of  $r = -0.45$ . These results suggest that our objects mainly have a secondary nitrogen production together with some other mechanisms that deviate them from the usual theoretical secondary curve and from the observational sequence of H II regions. We explore several mechanisms proposed in the literature to explain these deviations. We did not find any evidence to support the reported mechanisms. We also investigated the existence of N/O abundance dependence with the stellar masses of the hosting galaxies and we did not find any correlation between these two parameters.

## ACKNOWLEDGEMENTS

CBO is grateful to the Fundação de Amparo à Pesquisa do Estado de São Paulo (FAPESP) for the support under grant 2019/11934-0 and to the Coordenação de Aperfeiçoamento de Pessoal de Nível Superior (CAPES). ACK thanks to FAPESP for the support grant 2020/16416-5 and to Conselho Nacional de Desenvolvimento Científico e Tecnológico (CNPq). OLD is grateful to FAPESP and CNPq. JAHJ acknowledges support from FAPESP, process number 2021/08920-8. GSI acknowledges financial support from FAPESP (Proj. 2022/11799-9).

## DATA AVAILABILITY

The data underlying this article will be shared on reasonable request to the corresponding author.

## REFERENCES

- Agostino C. J., Salim S., 2019, *ApJ*, **876**, 12  
 Allende Prieto C., Lambert D. L., Asplund M., 2001, *ApJ*, **556**, L63  
 Aller L. H., Liller W., 1968, in Middlehurst B. M., Aller L. H., eds., *Nebulae and Interstellar Matter*. University of Chicago Press, p. 483  
 Alloin D., Collin-Souffrin S., Joly M., Vigroux L., 1979, *A&A*, **78**, 200  
 Andrews B. H., Martini P., 2013, *ApJ*, **765**, 140  
 Annibali F., Bressan A., Rampazzo R., Zeilinger W. W., Vega O., Panuzzo P., 2010, *A&A*, **519**, A40  
 Arellano-Córdova K. Z., et al., 2022, *ApJ*, **940**, L23  
 Armah M., et al., 2021, *MNRAS*, **508**, 371  
 Armah M., et al., 2023, *MNRAS*, **520**, 1687  
 Baldwin J. A., Phillips M. M., Terlevich R., 1981, *PASP*, **93**, 5  
 Bär R. E., Weigel A. K., Sartori L. F., Oh K., Koss M., Schawinski K., 2017, *MNRAS*, **466**, 2879  
 Belfiore F., et al., 2015, *MNRAS*, **449**, 867  
 Belfiore F., et al., 2017, *MNRAS*, **469**, 151  
 Berg D. A., Skillman E. D., Croxall K. V., Pogge R. W., Moustakas J., Johnson-Groh M., 2015, *ApJ*, **806**, 16  
 Berg D. A., Erb D. K., Henry R. B. C., Skillman E. D., McQuinn K. B. W., 2019, *ApJ*, **874**, 93  
 Berg D. A., Pogge R. W., Skillman E. D., Croxall K. V., Moustakas J., Rogers N. S. J., Sun J., 2020, *ApJ*, **893**, 96  
 Binette L., Matadamas R., Hägele G. F., Nicholls D. C., Magris C. G., Peña-Guerrero M. Á., Morisset C., Rodríguez-González A., 2012, *A&A*, **547**, A29  
 Blanc G. A., Heiderman A., Gebhardt K., Evans Neal J. I., Adams J., 2009, *ApJ*, **704**, 842

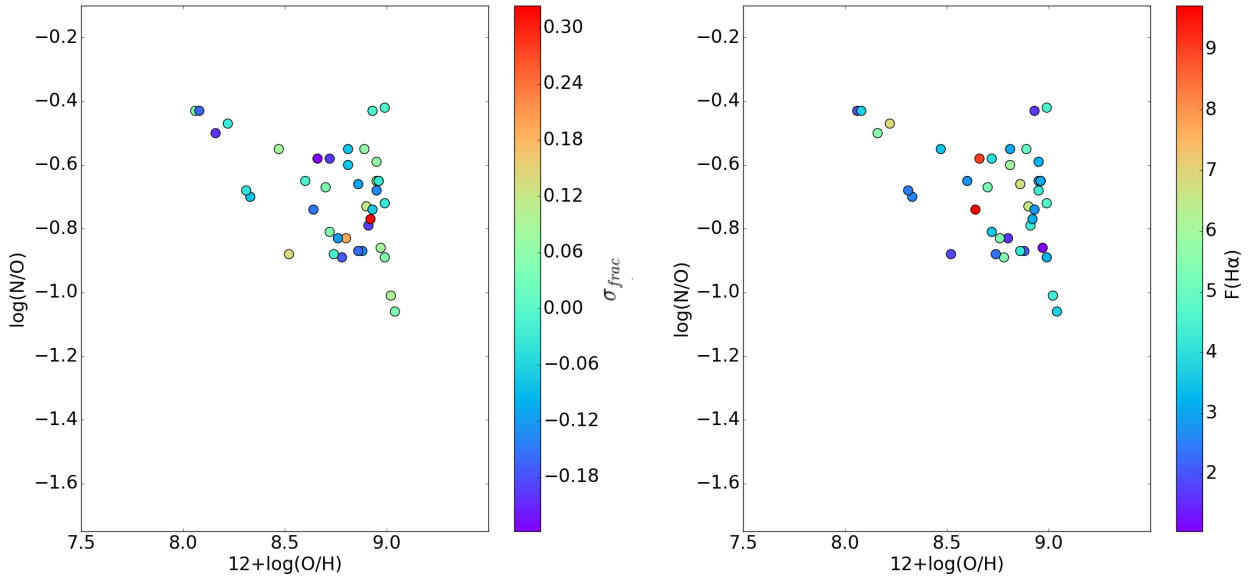


**Figure 6.**  $\log(\text{N/O})$  vs.  $12+\log(\text{O/H})$  diagram. The color bars indicate the  $\sigma_{\text{frac}}$  value (left panel) and the  $\text{H}\alpha$  fluxes in units of  $10^{-17}$  erg/s/cm<sup>2</sup>/spaxel (right panel) for each object in our sample.

**Table 3.** Number of objects of each sample (N), median values and ranges for O/H and N/O abundances for each study: SF galaxies reported by Zinchenko et al. (2021); Seyfert 2 nuclei analyzed by Dors et al. (2017), LINER galaxies studied by Pérez-Díaz et al. (2021), and LINERs analyzed in this work. Fitted equations for each sample, being  $x = 12 + \log(\text{O/H})$  and  $y = \log(\text{N/O})$ , as well as Pearson's correlation coefficient, are also shown.

Reference	N	12+log(O/H)		log(N/O)		Fitted equation	Correlation Coefficient (r)
		Median	Range	Median	Range		
Zinchenko et al. (2021)	1431	$8.57 \pm 0.12$	7.93, 8.81	$-0.86 \pm 0.22$	-1.48, -0.24	$y = 1.80x^2 - 28.91x + 114.50$	0.92
Berg et al. (2020)	176	$8.52 \pm 0.20$	7.81, 8.96	$-0.92 \pm 0.24$	-1.46, -0.42	$y = 0.67x - 6.61$	0.54
Dors et al. (2017)	44	$8.65 \pm 0.19$	8.07, 8.97	$-0.54 \pm 0.12$	-0.80, -0.29	$y = 0.05x - 0.97$	0.08
Pérez-Díaz et al. (2021)	65	$8.57 \pm 0.24$	8.01, 8.86	$-0.61 \pm 0.20$	-1.11, -0.21	$y = -0.34x + 2.33$	-0.42
This work	40	$8.83 \pm 0.27$	8.05, 9.03	$-0.69 \pm 0.16$	-1.05, -0.42	$y = -0.26x + 1.66$	-0.45

Brinchmann J., Charlot S., Kauffmann G., Heckman T., White S. D. M., Tremonti C., 2013, *MNRAS*, **432**, 2112  
Brown J. S., Martini P., Andrews B. H., 2016, *MNRAS*, **458**, 1529  
Bundy K., et al., 2015, *ApJ*, **798**, 7  
Byler N., Dalcanton J. J., Conroy C., Johnson B. D., Choi J., Dotter A., Rosenfield P., 2019, *AJ*, **158**, 2  
Cardelli J. A., Clayton G. C., Mathis J. S., 1989, *ApJ*, **345**, 245  
Carvalho S. P., et al., 2020, *MNRAS*, **492**, 5675  
Castaneda H. O., Vilchez J. M., Copetti M. V. F., 1992, *A&A*, **260**, 370  
Castro C. S., Dors O. L., Cardaci M. V., Hägele G. F., 2017, *MNRAS*, **467**, 1507  
Cedrés B., Beckman J. E., Bongiovanni Á., Cepa J., Asensio Ramos A., Giammanco C., Cabrera-Lavers A., Alfaro E. J., 2013, *ApJ*, **765**, L24  
Charlot S., Longhetti M., 2001, *MNRAS*, **323**, 887  
Christensen T., Petersen L., Gammelgaard P., 1997, *A&A*, **322**, 41  
Cid Fernandes R., Stasińska G., Schlickmann M. S., Mateus A., Vale Asari N., Schoenell W., Sodré L., 2010, *MNRAS*, **403**, 1036  
Cid Fernandes R., Stasińska G., Mateus A., Vale Asari N., 2011, *MNRAS*, **413**, 1687  
Congiu E., et al., 2017, *MNRAS*, **471**, 562  
Constantin A., Shields J. C., Ho L. C., Barth A. J., Filippenko A. V., Castillo C. A., 2015, *ApJ*, **814**, 149  
Contini M., 2017, *MNRAS*, **469**, 3125  
Copetti M. V. F., Mallmann J. A. H., Schmidt A. A., Castañeda H. O., 2000,

*A&A*, **357**, 621  
Curti M., Cresci G., Mannucci F., Marconi A., Maiolino R., Esposito S., 2017, *MNRAS*, **465**, 1384  
Curti M., et al., 2023, *MNRAS*, **518**, 425  
Davies R. L., et al., 2017, *MNRAS*, **470**, 4974  
Díaz A. I., Pérez-Montero E., 2000, *MNRAS*, **312**, 130  
Díaz Á. I., Zamora S., 2022, *MNRAS*, **511**, 4377  
Díaz Á. I., Terlevich E., Castellanos M., Hägele G. F., 2007, *MNRAS*, **382**, 251  
Dopita M. A., Sutherland R. S., Nicholls D. C., Kewley L. J., Vogt F. P. A., 2013, *ApJS*, **208**, 10  
Dors O. L., 2021, *MNRAS*, **507**, 466  
Dors O. L. J., Copetti M. V. F., 2005, *A&A*, **437**, 837  
Dors O. L., Copetti M. V. F., 2006, *A&A*, **452**, 473  
Dors O. L., Storchi-Bergmann T., Riffel R. A., Schimdt A. A., 2008, *A&A*, **482**, 59  
Dors O. L., Krabbe A., Hägele G. F., Pérez-Montero E., 2011, *MNRAS*, **415**, 3616  
Dors O. L., Arellano-Córdova K. Z., Cardaci M. V., Hägele G. F., 2017, *MNRAS*, **468**, L113  
Dors O. L., Agarwal B., Hägele G. F., Cardaci M. V., Rydberg C.-E., Riffel R. A., Oliveira A. S., Krabbe A. C., 2018, *MNRAS*, **479**, 2294  
Dors O. L., Maiolino R., Cardaci M. V., Hägele G. F., Krabbe A. C., Pérez-Montero E., Armah M., 2020, *MNRAS*, **496**, 3209

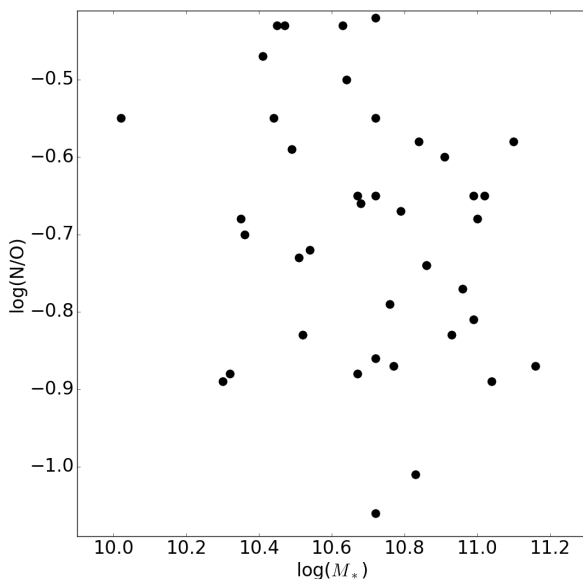


**Figure 7.**  $\log(M_*/M_\odot)$  vs.  $\log(\text{N/O})$ . The mass corresponds to the stellar masses of the hosting galaxies of our sample and is taken from the `manga.Pipe3D` and `manga.drpd` database (Sánchez et al. 2016). The N/O abundance is taken from Table 2.

Dors O. L., Contini M., Riffel R. A., Pérez-Montero E., Krabbe A. C., Cardaci M. V., Hägele G. F., 2021, *MNRAS*, **501**, 1370  
Dors O. L., et al., 2022, *MNRAS*, **514**, 5506  
Dors O. L., et al., 2023, *MNRAS*, **521**, 1969  
Edmunds M. G., Pagel B. E. J., 1978, *MNRAS*, **185**, 77P  
Esteban C., Peimbert M., Torres-Peimbert S., Escalante V., 1998, *MNRAS*, **295**, 401  
Feltre A., Charlot S., Gutkin J., 2016, *MNRAS*, **456**, 3354  
Feltre A., et al., 2023, *arXiv e-prints*, p. [arXiv:2301.02252](https://arxiv.org/abs/2301.02252)  
Ferland G. J., et al., 2017, *Rev. Mex. Astron. Astrofis.*, **53**, 385  
Fierro J., Torres-Peimbert S., Peimbert M., 1986, *PASP*, **98**, 1032  
Florido E., Zurita A., Pérez-Montero E., 2022, *MNRAS*, **513**, 2006  
Flury S. R., Moran E. C., 2020, *MNRAS*, **496**, 2191  
Freitas I. C., et al., 2018, *MNRAS*, **476**, 2760  
Garnett D. R., Dufour R. J., Peimbert M., Torres-Peimbert S., Shields G. A., Skillman E. D., Terlevich E., Terlevich R. J., 1995, *ApJ*, **449**, L77  
Grevesse N., Sauval A. J., 1998, *Space Sci. Rev.*, **85**, 161  
Grisoni V., Matteucci F., Romano D., 2021, *MNRAS*, **508**, 719  
Groves B. A., Dopita M. A., Sutherland R. S., 2004, *ApJS*, **153**, 9  
Hägele G. F., Pérez-Montero E., Díaz Á. I., Terlevich E., Terlevich R., 2006, *MNRAS*, **372**, 293  
Hägele G. F., Díaz Á. I., Terlevich E., Terlevich R., Pérez-Montero E., Cardaci M. V., 2008, *MNRAS*, **383**, 209  
Hägele G. F., García-Benito R., Pérez-Montero E., Díaz Á. I., Cardaci M. V., Firpo V., Terlevich E., Terlevich R., 2011, *MNRAS*, **414**, 272  
Hägele G. F., Firpo V., Bosch G., Díaz Á. I., Morrell N., 2012, *MNRAS*, **422**, 3475  
Henry R. B. C., Edmunds M. G., Köppen J., 2000, *ApJ*, **541**, 660  
Hirschauer A. S., Salzer J. J., Janowiecki S., Wegner G. A., 2018, *AJ*, **155**, 82  
Ho I. T., 2019, *MNRAS*, **485**, 3569  
Ho L. C., Filippenko A. V., Sargent W. L., 1995, *ApJS*, **98**, 477  
Ho L. C., Filippenko A. V., Sargent W. L. W., 1997, *ApJS*, **112**, 315  
Holweger H., 2001, in Wimmer-Schweingruber R. F., ed., *American Institute of Physics Conference Series* Vol. 598, Joint SOHO/ACE workshop “Solar and Galactic Composition”. pp 23–30

([arXiv:astro-ph/0107426](https://arxiv.org/abs/astro-ph/0107426)), doi:10.1063/1.1433974

Ilha G. S., et al., 2019, *MNRAS*, **484**, 252  
Izotov Y. I., Thuan T. X., 1999, *ApJ*, **511**, 639  
Izotov Y. I., Stasińska G., Meynet G., Guseva N. G., Thuan T. X., 2006, *A&A*, **448**, 955  
Izotov Y. I., Guseva N. G., Fricke K. J., Henkel C., 2019, *A&A*, **623**, A40  
Jenkins E. B., 1987, in Hollenbach D. J., Thronson Harley A. J., eds, Vol. 134, *Interstellar Processes*. p. 533, doi:10.1007/978-94-009-3861-8\_20  
Jenkins E., 1989, in Allamandola L. J., Tielens A. G. G. M., eds, Vol. 135, *Interstellar Dust*. p. 23  
Jiang T., Malhotra S., Rhoads J. E., Yang H., 2019, *ApJ*, **872**, 145  
Jin Y., Kewley L. J., Sutherland R. S., 2022, *ApJ*, **934**, L8  
Johansson J., Woods T. E., Gilfanov M., Sarzi M., Chen Y.-M., Oh K., 2016, *MNRAS*, **461**, 4505  
Johnson J. A., 2019, *Science*, **363**, 474  
Johnson J. W., Weinberg D. H., Vincenzo F., Bird J. C., Griffith E. J., 2023, *MNRAS*, **520**, 782  
Jones T., Martin C., Cooper M. C., 2015, *ApJ*, **813**, 126  
Juneau S., Dickinson M., Alexander D. M., Salim S., 2011, *ApJ*, **736**, 104  
Kakkad D., et al., 2018, *A&A*, **618**, A6  
Kauffmann G., et al., 2003, *MNRAS*, **346**, 1055  
Kennicutt Robert C. J., Bresolin F., Garnett D. R., 2003, *ApJ*, **591**, 801  
Kewley L. J., Dopita M. A., 2002, *ApJS*, **142**, 35  
Kewley L. J., Dopita M. A., Sutherland R. S., Heisler C. A., Trevena J., 2001, *ApJ*, **556**, 121  
Kewley L. J., Nicholls D. C., Sutherland R. S., 2019, *ARA&A*, **57**, 511  
Konstantopoulou C., et al., 2023, *arXiv e-prints*, p. [arXiv:2310.07709](https://arxiv.org/abs/2310.07709)  
Krabbe A. C., Oliveira C. B. J., Zinchenko I. A., Hernández-Jiménez J. A., O. L. Dors J., Hägele G. F., Cardaci M. V., Telles N. R., 2021, *MNRAS*, **508**, 3793  
Kumari N., James B. L., Irwin M. J., Amorín R., Pérez-Montero E., 2018, *MNRAS*, **476**, 3793  
Kumari N., Maiolino R., Belfiore F., Curti M., 2019, *MNRAS*, **485**, 367  
Lagos P., et al., 2022, *MNRAS*, **516**, 5487  
López-Sánchez Á. R., Esteban C., 2008, *A&A*, **491**, 131  
Maciel W. J., Pottasch S. R., 1982, *A&A*, **106**, 1  
Magrini L., et al., 2018, *A&A*, **618**, A102  
Maiolino R., Mannucci F., 2019, *A&ARv*, **27**, 3  
Marino R. A., et al., 2013, *A&A*, **559**, A114  
Martín-Doménech R., Jiménez-Serra I., Muñoz Caro G. M., Müller H. S. P., Occhiogrosso A., Testi L., Woods P. M., Viti S., 2016, *A&A*, **585**, A112  
Matteucci F., 1986, *MNRAS*, **221**, 911  
McGaugh S. S., 1991, *ApJ*, **380**, 140  
Mesa-Delgado A., Esteban C., 2010, *MNRAS*, **405**, 2651  
Mesa-Delgado A., Núñez-Díaz M., Esteban C., López-Martín L., García-Rojas J., 2011, *MNRAS*, **417**, 420  
Metha B., Trenti M., Chu T., Battisti A., 2022, *MNRAS*, **514**, 4465  
Meyer D. M., Jura M., Cardelli J. A., 1998, *ApJ*, **493**, 222  
Meynet G., Maeder A., 2002, *A&A*, **381**, L25  
Mingozzi M., et al., 2019, *A&A*, **622**, A146  
Mingozzi M., et al., 2020, *A&A*, **636**, A42  
Monteiro A. F., Dors O. L., 2021, *MNRAS*, **508**, 3023  
Morales-Luis A. B., Pérez-Montero E., Sánchez Almeida J., Muñoz-Tuñón C., 2014, *ApJ*, **797**, 81  
Nagao T., Maiolino R., Marconi A., 2006, *A&A*, **459**, 85  
Netzer H., 2013, *The Physics and Evolution of Active Galactic Nuclei*. Cambridge University Press, doi:10.1017/CBO9781139109291  
Nicholls D. C., Dopita M. A., Sutherland R. S., 2012, *ApJ*, **752**, 148  
O’Dell C. R., Ferland G. J., Peimbert M., 2017, *MNRAS*, **464**, 4835  
Oey M. S., Shields J. C., 2000, *ApJ*, **539**, 687  
Oey M. S., et al., 2007, *ApJ*, **661**, 801  
Oliveira C. B., Krabbe A. C., Hernández-Jiménez J. A., Dors O. L., Zinchenko I. A., Hägele G. F., Cardaci M. V., Monteiro A. F., 2022, *MNRAS*, **515**, 6093  
Osterbrock D. E., 1970, *QJRAS*, **11**, 199  
Osterbrock D. E., 1974, *Astrophysics of gaseous nebulae*. University Science Books  
Osterbrock D. E., 1989, *Astrophysics of gaseous nebulae and active galactic nuclei*. University Science Books

- Osterbrock D., Flather E., 1959, *ApJ*, **129**, 26
- Pagel B. E. J., Edmunds M. G., Blackwell D. E., Chun M. S., Smith G., 1979, *MNRAS*, **189**, 95
- Panuzzo P., Rampazzo R., Bressan A., Vega O., Annibali F., Buson L. M., Clemens M. S., Zeilinger W. W., 2011, *A&A*, **528**, A10
- Peimbert M., 1967, *ApJ*, **150**, 825
- Peimbert M., 1975, *ARA&A*, **13**, 113
- Peimbert M., Costero R., 1969, Boletín de los Observatorios Tonantzintla y Tacubaya, **5**, 3
- Peimbert A., Peimbert M., 2010, *ApJ*, **724**, 791
- Peimbert M., Peimbert A., Delgado-Inglada G., 2017, *PASP*, **129**, 082001
- Pérez-Díaz B., Masegosa J., Márquez I., Pérez-Montero E., 2021, *MNRAS*, **505**, 4289
- Pérez-Montero E., 2014, *MNRAS*, **441**, 2663
- Pérez-Montero E., 2017, *PASP*, **129**, 043001
- Pérez-Montero E., Contini T., 2009, *MNRAS*, **398**, 949
- Pérez-Montero E., Díaz A. I., 2005, *MNRAS*, **361**, 1063
- Pérez-Montero E., Díaz A. I., Vílchez J. M., Kehrig C., 2006, *A&A*, **449**, 193
- Pérez-Montero E., García-Benito R., Hägele G. F., Díaz Á. I., 2010, *MNRAS*, **404**, 2037
- Pérez-Montero E., Dors O. L., Vílchez J. M., García-Benito R., Cardaci M. V., Hägele G. F., 2019, *MNRAS*, **489**, 2652
- Pérez-Montero E., Amorín R., Sánchez Almeida J., Vílchez J. M., García-Benito R., Kehrig C., 2021, *MNRAS*, **504**, 1237
- Pérez-Montero E., Zinchenko I. A., Vílchez J. M., Zurita A., Florido E., Pérez-Díaz B., 2023, *A&A*, **669**, A88
- Pettini M., Pagel B. E. J., 2004, *MNRAS*, **348**, L59
- Pilyugin L. S., 2003, *A&A*, **399**, 1003
- Pilyugin L. S., Grebel E. K., 2016, *MNRAS*, **457**, 3678
- Pilyugin L. S., Thuan T. X., Vílchez J. M., 2003, *A&A*, **397**, 487
- Pilyugin L. S., Vílchez J. M., Contini T., 2004, *A&A*, **425**, 849
- Pilyugin L. S., Thuan T. X., Vílchez J. M., 2007, *MNRAS*, **376**, 353
- Pilyugin L. S., Grebel E. K., Mattsson L., 2012, *MNRAS*, **424**, 2316
- Pović M., Márquez I., Netzer H., Masegosa J., Nordon R., Pérez E., Schoenell W., 2016, *MNRAS*, **462**, 2878
- Rauch T., 2003, *A&A*, **403**, 709
- Rayo J. F., Peimbert M., Torres-Peimbert S., 1982, *ApJ*, **255**, 1
- Revalski M., Crenshaw D. M., Kraemer S. B., Fischer T. C., Schmitt H. R., Machuca C., 2018a, *ApJ*, **856**, 46
- Revalski M., et al., 2018b, *ApJ*, **867**, 88
- Revalski M., et al., 2021, *ApJ*, **910**, 139
- Ricci T. V., Steiner J. E., Menezes R. B., 2014, *MNRAS*, **440**, 2419
- Rich J. A., Kewley L. J., Dopita M. A., 2014, *ApJ*, **781**, L12
- Riffel R. A., Dors O. L., Krabbe A. C., Esteban C., 2021, *MNRAS*, **506**, L11
- Rogers N. S. J., Skillman E. D., Pogge R. W., Berg D. A., Croxall K. V., Bartlett J., Arellano-Córdova K. Z., Moustakas J., 2022, *ApJ*, **939**, 44
- Ruschel-Dutra D., et al., 2021, *MNRAS*, **507**, 74
- Salim S., Narayanan D., 2020, *ARA&A*, **58**, 529
- Sánchez S. F., et al., 2012, *A&A*, **538**, A8
- Sánchez S. F., et al., 2014, *A&A*, **563**, A49
- Sánchez S. F., et al., 2016, *Rev. Mex. Astron. Astrofis.*, **52**, 171
- Sanders R. L., Shapley A. E., Topping M. W., Reddy N. A., Brammer G. B., 2023, *arXiv e-prints*, p. arXiv:2303.08149
- Seaton M. J., 1960, *MNRAS*, **120**, 326
- Shi F., Zhao G., Liang Y. C., 2007, *A&A*, **475**, 409
- Shirazi M., Brinchmann J., 2012, *MNRAS*, **421**, 1043
- Smee S. A., et al., 2013, *AJ*, **146**, 32
- Sofía U. J., Cardelli J. A., Savage B. D., 1994, *ApJ*, **430**, 650
- Stasińska G., 2006, *A&A*, **454**, L127
- Stasińska G., et al., 2008, *MNRAS*, **391**, L29
- Storchi-Bergmann T., Schmitt H. R., Calzetti D., Kinney A. L., 1998, *The AJ*, **115**, 909
- Talbot R. J., Arnett D. W., 1974, *ApJ*, **190**, 605
- Talent D. L., Dufour R. J., 1979, *ApJ*, **233**, 888
- Thomas A. D., Kewley L. J., Dopita M. A., Groves B. A., Hopkins A. M., Sutherland R. S., 2019, *ApJ*, **874**, 100
- Thuan T. X., Pilyugin L. S., Zinchenko I. A., 2010, *ApJ*, **712**, 1029
- Thurston T. R., Edmunds M. G., Henry R. B. C., 1996, *MNRAS*, **283**, 990
- Toribio San Cipriano L., Domínguez-Guzmán G., Esteban C., García-Rojas J., Mesa-Delgado A., Bresolin F., Rodríguez M., Simón-Díaz S., 2017, *MNRAS*, **467**, 3759
- Tremonti C. A., et al., 2004, *ApJ*, **613**, 898
- Truran J. W., Cameron A. G. W., 1971, *Ap&SS*, **14**, 179
- Veilleux S., Osterbrock D. E., 1987, *ApJS*, **63**, 295
- Viironen K., Delgado-Inglada G., Mampaso A., Magrini L., Corradi R. L. M., 2007, *MNRAS*, **381**, 1719
- Vincenzo F., Kobayashi C., 2018, *A&A*, **610**, L16
- Vincenzo F., Belfiore F., Maiolino R., Matteucci F., Ventura P., 2016, *MNRAS*, **458**, 3466
- Wake D. A., et al., 2017, *AJ*, **154**, 86
- Woods T. E., Gilfanov M., 2013, *MNRAS*, **432**, 1640
- Wu Y.-Z., Zhang S.-N., 2013, *MNRAS*, **436**, 934
- Wylezalek D., Zakamska N. L., Greene J. E., Riffel R. A., Drory N., Andrews B. H., Merloni A., Thomas D., 2018, *MNRAS*, **474**, 1499
- Yin S. Y., Liang Y. C., Hammer F., Brinchmann J., Zhang B., Deng L. C., Flores H., 2007, *A&A*, **462**, 535
- York D. G., et al., 2000, *AJ*, **120**, 1579
- Zhang K., et al., 2017, *MNRAS*, **466**, 3217
- Zinchenko I. A., 2023, *A&A*, **674**, L7
- Zinchenko I. A., Pilyugin L. S., 2022, *Astronomische Nachrichten*, **343**, e20220048
- Zinchenko I. A., Vílchez J. M., Pérez-Montero E., Sukhorukov A. V., Sobolenko M., Duarte Puertas S., 2021, *A&A*, **655**, A58
- do Nascimento J. C., et al., 2022, *MNRAS*, **513**, 807
- van Hoof P. A. M., 1997, PhD thesis, Rijksuniversiteit Groningen
- van Hoof P. A. M., Weingartner J. C., Martin P. G., Volk K., Ferland G. J., 2001, in Ferland G., Savin D. W., eds, *Astronomical Society of the Pacific Conference Series Vol. 247, Spectroscopic Challenges of Photoionized Plasmas*. p. 363 ([arXiv:astro-ph/0107183](https://arxiv.org/abs/astro-ph/0107183)), doi:10.48550/arXiv.astro-ph/0107183
- van Zee L., Salzer J. J., Haynes M. P., O'Donoghue A. A., Balonek T. J., 1998, *AJ*, **116**, 2805

This paper has been typeset from a  $\text{\TeX}/\text{\LaTeX}$  file prepared by the author.